Simulation of the interaction of light with 3-D metallic nanostructures using a proper orthogonal decomposition-Galerkin reduced-order discontinuous Galerkin time-domain method

Kun Li, Ting-zhu Huang, Liang Li, Stéphane Lanteri

Simulation of the interaction of light with 3-D metallic nanostructures using a POD-Galerkin reduced-order DGTD method

Kun Li[a], Ting-Zhu Huang[b,*], Liang Li[b,*], Stéphane Lanteri[c]

[a] *School of Mathematics, Southwestern University of Finance and Economics, Chengdu, P.R. China*
[b] *School of Mathematical Sciences, University of Electronic Science and Technology of China, Chengdu, P.R. China*
[c] *Université Côte d'Azur, Inria, CNRS, LJAD, Sophia Antipolis Cedex, France*

Abstract

In this work we report on a reduced-order model (ROM) based on the proper orthogonal decomposition (POD) technique for the system of 3-D time-domain Maxwell's equations coupled to a Drude dispersion model, which is employed to describe the interaction of light with nanometer scale metallic structures. By using the singular value decomposition (SVD) method, the POD basis vectors are extracted offline from the snapshots produced by a high order discontinuous Galerkin time-domain (DGTD) solver. With a Galerkin projection and a second order leap-frog (LF_2) time discretization, a discrete ROM is constructed. The stability condition of the ROM is then analyzed. In particular, when the boundary is a perfect electric conductor condition, the global energy of the ROM is bounded, which is consistent with the characteristics of global energy in the DGTD method. It is shown that the ROM based on Galerkin projection can maintain the stability characteristics of the original high dimensional model. Numerical experiments are presented to verify the accuracy, demonstrate the capabilities of the POD-based ROM and assess its efficiency for 3-D nanophotonic problems.

Keywords: Discontinuous Galerkin time-domain method, model order reduction, proper orthogonal decomposition, stability analysis, metallic nanostructures

1. Introduction

Nano-Plasmonics is an active field of research concerned with the study of the interaction of light with metallic nanostructures [1], leading to resonant oscillations of the conduction-band electrons at the metal surface [2], typically depending on the frequency and polarization characteristics of incident light as well as on geometrical and compositional factors [3]. These resonances can both enhance and confine optical fields [4]. Many attractive and/or potential applications [1, 5], e.g., sub-wavelength imaging, invisibility cloaking, nano antennas, chemical biosensors, metamaterials, plasmon waveguides, and magnetic storage media, leverage this local field enhancement. From the mathematical modeling point of view, these applications require to solve the system of Maxwell's equations coupled to an appropriate mathematical model of physical dispersion for characterizing the material properties of the involved metallic nanostructures at optical frequencies [1, 4], such as the Drude model [6, 7], the nonlocal hydrodynamic Drude model [8], and the generalized nonlocal optical response model [9].

*Corresponding author
Email addresses: rclikun@163.com, likun@swufe.edu.cn (Kun Li), tzhuang@uestc.edu.cn (Ting-Zhu Huang), plum_liliang@uestc.edu.cn, plum.liliang@gmail.com (Liang Li), Stephane.Lanteri@inria.fr (Stéphane Lanteri)

Several numerical methods have been developed for computing the numerical solution of the time-domain Maxwell's equations. Finite difference time-domain (FDTD) algorithm [10] proposed by K.S. Yee in 1966 is the most widely used approach among physicists and engineers due to its simplicity and efficiency. In this method, the whole computational domain is discretized using a structured (Cartesian) grid. However, FDTD methd poorly perform when facing the modeling difficulties that are inherent to realistic nanophotonic applications, in particular in the presence of curved geometries of the considered nanostructures, because Cartesian grids can only approximate these irregular boundaries in a stair-cased manner [11]. In this context some more flexible methods based on unstructured and possibly non-conforming meshes are particularly attractive. This is for instance the case with discontinuous Galerkin (DG) schemes. A discontinuous Galerkin time-domain (DGTD) method can be seen as a mix of the finite element (FE, spaces of basis and test functions are defined) and finite volume (FV, the neighboring elements are connected by numerical traces) type discretization methods [12], but generally performs better than both by exploiting their positive features [13]. In particular, the DGTD method has several attractive features, for example, easy adaptation to complex geometries and material composition [14], local approximation order strategy [15], as well as easy parallelism [16]. We note that DGTD method is increasingly used in the simulation of time-domain nanoscale light-matter interaction problems [12, 15, 17, 18, 19, 20, 21, 22, 23, 24].

Although the DGTD method is highly accurate and widely applicable, it forms a high-dimensional model (HDM) because of the duplication of the degrees of freedom (DoF) on the boundaries of the elements, typically several millions in large 3-D problems, which is greater than the number of DoF used by the FE type discretization method for the same level of accuracy [25]. Hence, it is attempting to develop a reduced-order modeling strategy for the DGTD scheme with a significantly smaller DoF but maintaining a sufficiently high accuracy, which will be then applicable to goal-oriented studies such as optimal design of nanostructures or propagation of modeling uncertainties [26]. Different kinds of reduced-order models (ROM) have been developed, such as simplified models and data-fit models [27, 28]. The alternative ROM that we consider in this study is a projection-based model, which proceeds by identifying a reduced subspace that is constructed to retain the essential character of the system input-output map [27]. There are many approaches for constructing the reduced subspace, see [29] for a detailed survey.

Proper orthogonal decomposition (POD) method, also known as Karhunen-Loeve expansions, principal component analysis, or singular value decomposition, is a popular basis generation approach for the reduced subspace [27, 30, 31, 32] because it is applicable to a wide range of problems, including time-dependent and nonlinear problems. The POD method with snapshots technique introduced by Sirovich [33] is probably the most widespread used to construct the ROM at least in terms of applications [2]. The POD method has widely been used in realistic numerical simulations [2, 32, 34, 35, 36, 37, 38, 39, 40, 41]. The starting point for POD method is a set of solutions, typically called *snapshots*, that are sampled offline from a high fidelity simulations or experiments at a number of time levels. ROM is created by constructing the reduced subspace composed of a set of low-dimensional POD basis vectors, which are generated by the snapshots, and seeking approximation solutions within this reduced subspace via Galerkin projection or other means. POD-Galerkin method combined with some numerical methods, such as finite difference (FD) [42, 43, 44], FE [45, 46, 47], FV [48, 49], and DG [26, 37] methods, has proved to be a powerful technique to save computational time for the time-domain partial differential equations (PDEs).

In this study, we couple a POD technique with a classical DGTD method (termed POD-DGTD) for the 3-D simulation of electromagnetic wave interaction with metallic nanostructures described by the Drude dispersion model, which is a sequel of [26], where we only studied the

Drude dispersion model for 2-D configurations. Here, the stability of the POD-based ROM equipped with a second order leap-frog (LF_2) method for time integration is analysed via an energy method in this article. In addition to this theoretical results, other contribution of this study is the numerical demonstration of the effectiveness of the combination of existing numerical approaches DGTD and POD, in dealing with the 3-D simulation of time-domain nanoscale light-matter interaction problems.

The rest of the paper is organized as follows. We briefly introduce the DG formulations for time-domain Maxwell's equations with the Durde model in Section 2. The POD-based ROM is established, and the stability of ROM equipped with LF_2 time scheme is analyzed in Section 3. In Section 4, we report some 3-D numerical results. We draw conclusions in Section 5.

2. DGTD formulations for the Drude model

Let $\Omega \in \mathcal{R}^3$ and $T_f > 0$ be a bounded convex polyhedral domain and a physical simulation time, respectively. Moreover, ε_r (resp. μ_r) is the relative electric permittivity (resp. magnetic permeability) parameter characterizing a homogeneous medium (e.g. vacuum, metal), ε_∞ represents the response from the bound ions and electrons of metal, ω_d is the plasma frequency of metal, and γ_d denotes the coefficient associated with the electron-ion and electron-electron collisions. In order to allow for the numerical treatment of metallic nanostructures, we consider the Drude dispersive model [6, 7], in which the frequency dependent permittivity is given by

$$\varepsilon_r(\omega) = \varepsilon_\infty - \frac{\omega_d^2}{\omega^2 + i\omega\gamma_d}, \tag{1}$$

where ω is the angular frequency. Such an optical model assumes that the electrons in the valence band are completely separated from the ions, and only the collision of electrons with electrons and ions is considered [11]. This model explains the dispersion and loss of metals and is often referred to as *local* model, because one assumes that the motion of an electron is not coupled to that of its neighbors [2, 12]. The normalized system of 3-D time-domain Maxwell's equations with the Drude dispersive properties based on the direct method (DM) or auxiliary differential equation (ADE) formulation is given by

$$\begin{cases} \partial_t \mathbf{H} & + & \nabla \times \mathbf{E} = 0, & \text{in } \Omega \times [0, T_f], \\ \varepsilon_\infty \partial_t \mathbf{E} & - & \nabla \times \mathbf{H} + \mathbf{J}_p = 0, & \text{in } \Omega \times [0, T_f], \\ \partial_t \mathbf{J}_p & + & \gamma_d \mathbf{J}_p - \omega_d^2 \mathbf{E} = 0, & \text{in } \Omega \times [0, T_f], \end{cases} \tag{2}$$

where the symbol ∂_t denotes a time derivate, $\mathbf{E}$, $\mathbf{H}$, and $\mathbf{J}_p$ respectively denote the electric field, magnetic field and dipolar current vector. The boundary of Ω is defined as $\partial\Omega = \Gamma_a \cup \Gamma_m$ with $\Gamma_a \cap \Gamma_m = \varnothing$. On the boundary $\partial\Omega$, we consider a perfect electric conductor (PEC) condition on Γ_m and a first order Silver-Müller absorbing boundary condition (ABC) on Γ_a

$$\begin{cases} \mathbf{n} \times \mathbf{E} = 0, & \text{on } \Gamma_m, \\ \mathbf{n} \times \mathbf{E} + z\mathbf{n} \times (\mathbf{n} \times \mathbf{H}) = \mathbf{n} \times \mathbf{E}^{\text{inc}} + z\mathbf{n} \times (\mathbf{n} \times \mathbf{H}^{\text{inc}}), & \text{on } \Gamma_a, \end{cases} \tag{3}$$

where $z = \sqrt{\mu_r/\varepsilon_r}$, $\mathbf{n}$ denotes the unit outward normal to $\partial\Omega$, and $(\mathbf{E}^{\text{inc}}, \mathbf{H}^{\text{inc}})$ denotes a given incident field. Finally, the system is supplemented with initial conditions $\mathbf{E}_0(\mathbf{x}) = \mathbf{E}(\mathbf{x}, 0)$, $\mathbf{H}_0(\mathbf{x}) = \mathbf{H}(\mathbf{x}, 0)$, and $\mathbf{J}_{p,0}(\mathbf{x}) = \mathbf{J}_p(\mathbf{x}, 0)$.

In a DG framework, the computational domain is divided into tetrahedra elements. Let $\mathcal{T}_h$ be a partition of the domain Ω using a set of elements K_i of size h_i, where $h_i = \text{diam}(K_i)$ is the diameter of the element K_i and $h = \max_{\forall i \in \mathcal{N}_\Omega} h_i$ with $\mathcal{N}_\Omega$ being the set of the indices of

elements. Then the DG method seeks an approximate solution $(\mathbf{E}_h, \mathbf{H}_h, \mathbf{J}_{p,h}) \in \mathbf{V}_h^p \times \mathbf{V}_h^p \times \mathbf{V}_h^p$ that satisfies for all local element K_i in $\mathcal{T}_h$ as follows [26]

$$\left\{\begin{array}{rcl} (\partial_t \mathbf{H}_h, \mathbf{v})_{K_i} & + & (\mathbf{E}_h, \mathrm{curl}\mathbf{v})_{K_i} - \langle \mathbf{E}_h^* \times \mathbf{n}, \mathbf{v}\rangle_{\partial K_i} = 0, \quad \forall \mathbf{v} \in \mathbf{V}_h, \\ (\varepsilon_\infty \partial_t \mathbf{E}_h, \mathbf{v})_{K_i} & - & (\mathbf{H}_h, \mathrm{curl}\mathbf{v})_{K_i} + (\mathbf{J}_{p,h}, \mathbf{v})_{K_i} + \langle \mathbf{H}_h^* \times \mathbf{n}, \mathbf{v}\rangle_{\partial K_i} = 0, \quad \forall \mathbf{v} \in \mathbf{V}_h, \\ (\partial_t \mathbf{J}_{p,h}, \mathbf{v})_{K_i} & + & (\gamma_d \mathbf{J}_{p,h}, \mathbf{v})_{K_i} - (\omega_d^2 \mathbf{E}_h, \mathbf{v})_{K_i} = 0, \quad \forall \mathbf{v} \in \mathbf{V}_h. \end{array}\right. \tag{4}$$

Here, $\mathbf{E}_h^*$ and $\mathbf{H}_h^*$ are the so-called numerical traces used to communicate information between adjacent elements [13, 50], and $\mathbf{V}_h$ denotes the discontinuous finite element space

$$\mathbf{V}_h = \{\mathbf{v} \in (L^2(\Omega))^3 \mid \mathbf{v}_{|K_i} \in (\mathbb{P}_{p_i}(K_i))^3, \ \forall i \in \mathcal{N}_\Omega\},$$

where $\mathbb{P}_{p_i}(K_i)$ is the space of nodal polynomials of degree at most p_i inside the element K_i. We choose to use the centered numerical traces [26]. By gathering the electric, magnetic and dipolar current vector DoF in each element into column vectors of size $N = 3\sum_{i\in\mathcal{N}_\Omega} d_i$ with d_i being the number of DoF inside K_i for each spatial dimension, one can deduce the following global semi-discrete system

$$\left\{\begin{array}{rcl} \mathbb{M}\partial_t \underline{\mathbf{H}}_h & = & -\mathbb{K}\underline{\mathbf{E}}_h + \mathbb{S}^i \underline{\mathbf{E}}_h + \mathbb{S}^e \widehat{\underline{\mathbf{E}}}_h + \mathbf{B}^e(t), \\ \varepsilon_\infty \mathbb{M}\partial_t \underline{\mathbf{E}}_h & = & \mathbb{K}\underline{\mathbf{H}}_h - \mathbb{S}^i \underline{\mathbf{H}}_h - \mathbb{S}^h \widehat{\underline{\mathbf{H}}}_h - \mathbb{M}\underline{\mathbf{J}}_{p,h} - \mathbf{B}^h(t), \\ \partial_t \underline{\mathbf{J}}_{p,h} & = & -\gamma_d \underline{\mathbf{J}}_{p,h} + \omega_d^2 \underline{\mathbf{E}}_h, \end{array}\right. \tag{5}$$

where $\widehat{\underline{\mathbf{E}}}_h = \underline{\mathbf{E}}_h$ and $\widehat{\underline{\mathbf{H}}}_h = \underline{\mathbf{H}}_h$ on a face of Γ_m; $\widehat{\underline{\mathbf{E}}}_h = \underline{\mathbf{H}}_h$ and $\widehat{\underline{\mathbf{H}}}_h = \underline{\mathbf{E}}_h$ on a face of Γ_a; $\mathbb{M}$ is a symmetric positive definite matrix, $\mathbb{K}$ and $\mathbb{S}^i$ are symmetric matrices, and $\mathbb{S}^e$ and $\mathbb{S}^h$ are skew-symmetric matrices. Besides, $\mathbb{S}^e = -\mathbb{S}^h$, $\mathbf{B}^h(t) = 0$, and $\mathbf{B}^e(t) = 0$ when $\Gamma_a = \varnothing$.

Remark 1. *Equipping with LF_2 time scheme for the global semi-discrete system* (5)*, one can define the following global discrete electromagnetic energy [19, 51] in the whole domain* Ω

$$\Theta^n = \frac{1}{2}[\varepsilon_\infty (\underline{\mathbf{E}}_h^{(n)})^T \mathbb{M}\underline{\mathbf{E}}_h^{(n)} + (\underline{\mathbf{H}}_h^{(n+\frac{1}{2})})^T \mathbb{M}\underline{\mathbf{H}}_h^{(n-\frac{1}{2})} + \frac{1}{\omega_d^2}(\underline{\mathbf{J}}_{p,h}^{(n+\frac{1}{2})})^T \mathbb{M}\underline{\mathbf{J}}_{p,h}^{(n-\frac{1}{2})}]. \tag{6}$$

Following the proof of stability [50, 52, 53], the global discrete electromagnetic energy (6) *with PEC only is a positive definite quadratic form of the numerical unknowns* $\underline{\mathbf{E}}_h^{(n)}$, $\underline{\mathbf{H}}_h^{(n-\frac{1}{2})}$, $\underline{\mathbf{H}}_h^{(n+\frac{1}{2})}$, $\underline{\mathbf{J}}_{p,h}^{(n-\frac{1}{2})}$, *and* $\underline{\mathbf{J}}_{p,h}^{(n+\frac{1}{2})}$ *if*

$$\Delta t < \min\{\frac{2\varepsilon_\infty}{d_N + 1}, \frac{2}{d_N}, \frac{2}{\gamma_d + 2\omega_d^2}\}, \tag{7}$$

with

$$d_N = \|\mathbb{M}^{-\frac{1}{2}}(\mathbb{K} - \mathbb{S}^i + \mathbb{S}^e)\mathbb{M}^{-\frac{1}{2}}\|,$$

where $\|\cdot\|$ *denote the canonical norm of a matrix, and* $(\cdot)^{-\frac{1}{2}}$ *is the inverse of the square root of a matrix.*

3. POD-based model order reduction

3.1. Reduced-order modeling

We equidistantly extract the ℓ snapshots from the full DGTD solutions. However, one may obtain the ensemble of snapshots from physical system trajectories by drawing samples from

experiments and interpolation (or data assimilation) [37, 48, 54]. We then formulate three snapshot matrices

$$\mathbf{A}_{\mathbf{u}} = \begin{pmatrix} \underline{\mathbf{u}}_{h,1}^{(n_1)} & \underline{\mathbf{u}}_{h,1}^{(n_2)} & \cdots & \underline{\mathbf{u}}_{h,1}^{(n_\ell)} \\ \underline{\mathbf{u}}_{h,2}^{(n_1)} & \underline{\mathbf{u}}_{h,2}^{(n_2)} & \cdots & \underline{\mathbf{u}}_{h,2}^{(n_\ell)} \\ \vdots & \vdots & \ddots & \vdots \\ \underline{\mathbf{u}}_{h,N}^{(n_1)} & \underline{\mathbf{u}}_{h,N}^{(n_2)} & \cdots & \underline{\mathbf{u}}_{h,N}^{(n_\ell)} \end{pmatrix} \in \mathcal{R}^{N\times\ell}, \quad \mathbf{u} \in \{\mathbf{E}, \mathbf{H}, \mathbf{J}_p\}.$$

Singular value decomposition (SVD) is applied to the snapshot matrices, and then the first $k_{\mathbf{u}}$ left singular vectors $\phi_{\mathbf{u},1}, \phi_{\mathbf{u},2}, \cdots, \phi_{\mathbf{u},k_{\mathbf{u}}}$ are selected to form the ROM basis [55]. Defining the associated basis matrix $\Phi_{\mathbf{u}} = (\phi_{\mathbf{u},1}, \phi_{\mathbf{u},2}, \cdots, \phi_{\mathbf{u},k_{\mathbf{u}}}) \in \mathcal{R}^{N\times k_{\mathbf{u}}}$ ($\mathbf{u} \in \{\mathbf{E}, \mathbf{H}, \mathbf{J}_p\}$), the approximate solutions of the fields $\underline{\mathbf{E}}_h$, $\underline{\mathbf{H}}_h$ and $\underline{\mathbf{J}}_{p,h}$ are obtained via following standard Galerkin ansatz

$$\underline{\mathbf{E}}_h \approx \underline{\mathbf{E}}_h^r = \Phi_{\mathbf{E}}\alpha_{\mathbf{E}}(t), \quad \underline{\mathbf{H}}_h \approx \underline{\mathbf{H}}_h^r = \Phi_{\mathbf{H}}\alpha_{\mathbf{H}}(t), \quad \text{and} \quad \underline{\mathbf{J}}_{p,h} \approx \underline{\mathbf{J}}_{p,h}^r = \Phi_{\mathbf{J}_p}\alpha_{\mathbf{J}_p}(t), \tag{8}$$

where $\alpha_{\mathbf{u}}(t) \in \mathcal{R}^{k_{\mathbf{u}}}$ and $\underline{\mathbf{u}}_h^r$ ($\mathbf{u} \in \{\mathbf{E}, \mathbf{H}, \mathbf{J}_p\}$) respectively denote the reduced solution and the approximate solution. With a Galerkin projection and a LF_2 time discretization, we have

$$\begin{cases} \varepsilon_\infty \Phi_{\mathbf{E}}^T \mathbb{M} \Phi_{\mathbf{E}} \dfrac{\alpha_{\mathbf{E}}^{(n+1)} - \alpha_{\mathbf{E}}^{(n)}}{\Delta t} &= \Phi_{\mathbf{E}}^T (\mathbb{K} - \mathbb{S}^i) \Phi_{\mathbf{H}} \alpha_{\mathbf{H}}^{(n+\frac{1}{2})} - \Phi_{\mathbf{E}}^T \mathbb{S}^h \widehat{\Phi}_{\mathbf{H}} \widehat{\alpha}_{\mathbf{H}}^{(n+\frac{1}{2})} \\ &- \Phi_{\mathbf{E}}^T \mathbb{M} \Phi_{\mathbf{J}_p} \alpha_{\mathbf{J}_p}^{(n+\frac{1}{2})} - \Phi_{\mathbf{E}}^T \mathbf{B}^h(n\Delta t), \\ \Phi_{\mathbf{H}}^T \mathbb{M} \Phi_{\mathbf{H}} \dfrac{\alpha_{\mathbf{H}}^{(n+\frac{3}{2})} - \alpha_{\mathbf{H}}^{(n+\frac{1}{2})}}{\Delta t} &= \Phi_{\mathbf{H}}^T (-\mathbb{K} + \mathbb{S}^i) \Phi_{\mathbf{E}} \alpha_{\mathbf{E}}^{(n+1)} + \Phi_{\mathbf{H}}^T \mathbb{S}^e \widehat{\Phi}_{\mathbf{E}} \widehat{\alpha}_{\mathbf{E}}^{(n+1)} \\ &+ \Phi_{\mathbf{H}}^T \mathbf{B}^e((n+\tfrac{1}{2})\Delta t), \\ \Phi_{\mathbf{J}_p}^T \mathbb{M} \Phi_{\mathbf{J}_p} \dfrac{\alpha_{\mathbf{J}_p}^{(n+\frac{3}{2})} - \alpha_{\mathbf{J}_p}^{(n+\frac{1}{2})}}{\Delta t} &= -\tfrac{\gamma_d}{2} \Phi_{\mathbf{J}_p}^T \mathbb{M} \Phi_{\mathbf{J}_p} (\alpha_{\mathbf{J}_p}^{(n+\frac{3}{2})} + \alpha_{\mathbf{J}_p}^{(n+\frac{1}{2})}) \\ &+ \omega_d^2 \Phi_{\mathbf{J}_p}^T \mathbb{M} \Phi_{\mathbf{E}} \alpha_{\mathbf{E}}^{(n+1)}, \end{cases} \tag{9}$$

with the initial conditions

$$\begin{cases} \alpha_{\mathbf{E}}^{(0)} = (\Phi_{\mathbf{E}}^T \mathbb{M} \Phi_{\mathbf{E}})^{-1} \Phi_{\mathbf{E}}^T \mathbb{M} \underline{\mathbf{E}}_h^{(0)}, \\ \alpha_{\mathbf{H}}^{(\frac{1}{2})} = (\Phi_{\mathbf{H}}^T \mathbb{M} \Phi_{\mathbf{H}})^{-1} \Phi_{\mathbf{H}}^T \mathbb{M} \underline{\mathbf{H}}_h^{(\frac{1}{2})}, \\ \alpha_{\mathbf{J}_p}^{(\frac{1}{2})} = (\Phi_{\mathbf{J}_p}^T \mathbb{M} \Phi_{\mathbf{J}_p})^{-1} \Phi_{\mathbf{J}_p}^T \mathbb{M} \underline{\mathbf{J}}_{p,h}^{(\frac{1}{2})}, \end{cases} \tag{10}$$

where $\widehat{\alpha}_{\mathbf{u}}(t)$ and $\widehat{\Phi}_{\mathbf{u}}$ ($\mathbf{u} = \mathbf{E}, \mathbf{H}$) are respectively defined by

$$\widehat{\alpha}_{\mathbf{E}}(t) = \begin{cases} \alpha_{\mathbf{E}}(t), & \text{if } F_h^B = \Gamma_m, \\ \alpha_{\mathbf{H}}(t), & \text{if } F_h^B = \Gamma_a, \end{cases} \quad \widehat{\alpha}_{\mathbf{H}}(t) = \begin{cases} \alpha_{\mathbf{H}}(t), & \text{if } F_h^B = \Gamma_m, \\ \alpha_{\mathbf{E}}(t), & \text{if } F_h^B = \Gamma_a, \end{cases}$$

and

$$\widehat{\Phi}_{\mathbf{E}} = \begin{cases} \Phi_{\mathbf{E}}, & \text{if } F_h^B = \Gamma_m, \\ \Phi_{\mathbf{H}}, & \text{if } F_h^B = \Gamma_a, \end{cases} \quad \widehat{\Phi}_{\mathbf{H}} = \begin{cases} \Phi_{\mathbf{H}}, & \text{if } F_h^B = \Gamma_m, \\ \Phi_{\mathbf{E}}, & \text{if } F_h^B = \Gamma_a. \end{cases}$$

Now, we summarize the offline and online stages for constructing the POD-based ROM in combination with the high order DGTD method for the numerical simulation of 3-D Maxwell's equations with the Drude dispersive model:

(1) Generate the snapshots (samples) ensemble $\mathbf{A}_{\mathbf{u}}$ ($\mathbf{u} \in \{\mathbf{E}, \mathbf{H}, \mathbf{J}_p\}$) from the full DGTD solutions.

(2) Set up the correlation matrix $\mathbf{C_u} = \mathbf{A_u}^T\mathbf{A_u} \in \mathcal{R}^{\ell\times\ell}$, and compute the eigenvalues $\lambda_{\mathbf{u},1} \geq \lambda_{\mathbf{u},2} \geq \cdots \geq \lambda_{\mathbf{u},r_\mathbf{u}} > 0$ and the corresponding orthogonal eigenvectors $\varphi_{\mathbf{u},1}, \varphi_{\mathbf{u},2}, \cdots, \varphi_{\mathbf{u},r_\mathbf{u}}$, where $r_\mathbf{u}$ is the rank of $\mathbf{A_u}$.

(3) Choose $k_\mathbf{u}$ to be the smallest integer such that

$$k_\mathbf{u} = \text{argmin}\{\mathcal{E}(k_\mathbf{u}) : \mathcal{E}(k_\mathbf{u}) \geq 1 - \rho\}, \tag{11}$$

where ρ is the truncation tolerance, and $\mathcal{E}(k_\mathbf{u}) = \sum_{i=1}^{k_\mathbf{u}} \lambda_{\mathbf{u},i} / \sum_{i=1}^{r_\mathbf{u}} \lambda_{\mathbf{u},i}$ denotes the relative information content [56].

(4) Compute the POD basis $\phi_{\mathbf{u},i} = \frac{1}{\sqrt{\lambda_{\mathbf{u},i}}}\mathbf{A_u}\varphi_{\mathbf{u},i}$ $(i = 1, 2, \cdots, k_\mathbf{u})$.

(5) Solve the fully discrete POD-based ROM (9) with the initial conditions (10) and get the reduced solutions $\alpha_\mathbf{E}^{(n)}$, $\alpha_\mathbf{H}^{(n+\frac{1}{2})}$ and $\alpha_{\mathbf{J}_p}^{(n+\frac{1}{2})}$.

(6) Expand the reduced solutions to the global solutions $\underline{\mathbf{E}}_h^{r,(n)}$, $\underline{\mathbf{H}}_h^{r,(n+\frac{1}{2})}$, and $\underline{\mathbf{J}}_{h,p}^{r,(n+\frac{1}{2})}$ based on (8).

Remark 2. *For $\forall X \in \mathcal{R}^{k_\mathbf{u}}$, and $X \neq 0$, one can get*

$$\Phi_\mathbf{u} X \neq 0, \quad \mathbf{u} \in \{\mathbf{E}, \mathbf{H}, \mathbf{J}_p\},$$

because $\Phi_\mathbf{u}$ consists of the left singular vectors corresponding to the $k_\mathbf{u}$ greatest singular values of $\mathbf{A_u}$. In addition, since $\mathbb{M}$ is a real symmetric positive definite matrix, we have

$$(\Phi_\mathbf{u}^T\mathbb{M}\Phi_\mathbf{u})^T = \Phi_\mathbf{u}^T\mathbb{M}\Phi_\mathbf{u},$$

and

$$X(\Phi_\mathbf{u}^T\mathbb{M}\Phi_\mathbf{u})X = (\Phi_\mathbf{u}X)^T\mathbb{M}(\Phi_\mathbf{u}X) > 0.$$

So, the matrix $\Phi_\mathbf{u}^T\mathbb{M}\Phi_\mathbf{u}$ is also a symmetric positive definite matrix in (9) *and* (10)*. In particular, the size of matrix $\Phi_\mathbf{u}^T\mathbb{M}\Phi_\mathbf{u}$ ($\mathbf{u} \in \{\mathbf{E}, \mathbf{H}, \mathbf{J}_p\}$) is very small, typically around 20 according to our numerical results, so the POD-DGTD method is still effective even if the matrix is dense.*

Remark 3. *The general goal is to reduce the complexity of a full time-domain simulation in order to address questions such design optimization or uncertainty quantification that will require performing many simulations. A specific goal is to study the applicability of POD for reducing the complexity of the full time-domain simulation and running with the same basis different configurations. The snapshot vectors in this paper are chosen from the full DGTD solutions. However, one may obtain the ensemble of snapshots from physical system trajectories by drawing samples from experiments and interpolation (or data assimilation) [37, 48, 54].*

3.2. Stability analysis

The stability of the POD-DGTD scheme with the LF_2 time scheme is now analyzed by using an energy method, where a quadratic form plays the role of a Lyapunov function of the whole set of numerical unknowns.

Definition 1. *We consider the following form of discrete energy in the whole domain Ω*

$$\Theta^{r,n} = \frac{1}{2}[\varepsilon_\infty(\underline{\mathbf{E}}_h^{r,(n)})^T\mathbb{M}\underline{\mathbf{E}}_h^{r,(n)} + (\underline{\mathbf{H}}_h^{r,(n+\frac{1}{2})})^T\mathbb{M}\underline{\mathbf{H}}_h^{r,(n-\frac{1}{2})} + \frac{1}{\omega_d^2}(\underline{\mathbf{J}}_{p,h}^{r,(n+\frac{1}{2})})^T\mathbb{M}\underline{\mathbf{J}}_{p,h}^{r,(n-\frac{1}{2})}]. \tag{12}$$

In the following, we shall prove that the discrete energy (12) is a positive definite quadratic form of all unknowns under a Courant-Friedrichs-Lewy (CFL)-type condition on the time step Δt.

Theorem 1. *Using the POD-DGTD scheme* (8)-(9) *when* $\Gamma_a = \varnothing$*, the global discrete energy* (12) *is a positive definite quadratic form of the unknowns* $\underline{\mathbf{E}}_h^r$*,* $\underline{\mathbf{H}}_h^r$ *and* $\underline{\mathbf{J}}_{p,h}^r$ *if*

$$\Delta t < \min\{\frac{2\varepsilon_\infty}{d_{N,1}^r + d_{N,2}^r}, \frac{2}{d_{N,1}^r}, \frac{2}{\gamma_d + 2\omega_d^2 d_{N,2}^r}\}, \tag{13}$$

with

$$d_{N,1}^r = \|(\Phi_{\mathbf{H}}^T \mathbb{M} \Phi_{\mathbf{H}})^{-\frac{1}{2}} \Phi_{\mathbf{H}}^T (\mathbb{K} - \mathbb{S}^i + \mathbb{S}^e) \Phi_{\mathbf{E}} (\Phi_{\mathbf{E}}^T \mathbb{M} \Phi_{\mathbf{E}})^{-\frac{1}{2}}\|,$$

and

$$d_{N,2}^r = \|(\Phi_{\mathbf{J}_p}^T \mathbb{M} \Phi_{\mathbf{J}_p})^{-\frac{1}{2}} \Phi_{\mathbf{J}_p}^T \mathbb{M} \Phi_{\mathbf{E}} (\Phi_{\mathbf{E}}^T \mathbb{M} \Phi_{\mathbf{E}})^{-\frac{1}{2}}\|.$$

Proof. Using the fully discrete POD-DGTD scheme (9) to develop $\alpha_{\mathbf{H}}^{(n+\frac{1}{2})}$ (resp. $\alpha_{\mathbf{J}_p}^{(n+\frac{1}{2})}$) in function of $\alpha_{\mathbf{H}}^{(n-\frac{1}{2})}$ and $\alpha_{\mathbf{E}}^{(n)}$ (resp. $\alpha_{\mathbf{J}_p}^{(n-\frac{1}{2})}$ and $\alpha_{\mathbf{E}}^{(n)}$) in (12), one can obtain

$$\begin{aligned}
\Theta^{r,n} &= \frac{1}{2}[\varepsilon_\infty (\alpha_{\mathbf{E}}^{(n)})^T \Phi_{\mathbf{E}}^T \mathbb{M} \Phi_{\mathbf{E}} \alpha_{\mathbf{E}}^{(n)} + (\alpha_{\mathbf{H}}^{(n+\frac{1}{2})})^T \Phi_{\mathbf{H}}^T \mathbb{M} \Phi_{\mathbf{H}} \alpha_{\mathbf{H}}^{(n-\frac{1}{2})} + \frac{1}{\omega_d^2} (\alpha_{\mathbf{J}_p}^{(n+\frac{1}{2})})^T \Phi_{\mathbf{J}_p}^T \mathbb{M} \Phi_{\mathbf{J}_p} \alpha_{\mathbf{J}_p}^{(n-\frac{1}{2})}] \\
&= \frac{1}{2}\varepsilon_\infty (\alpha_{\mathbf{E}}^{(n)})^T \Phi_{\mathbf{E}}^T \mathbb{M} \Phi_{\mathbf{E}} \alpha_{\mathbf{E}}^{(n)} + \frac{1}{2}(\alpha_{\mathbf{H}}^{(n-\frac{1}{2})})^T \Phi_{\mathbf{H}}^T \mathbb{M} \Phi_{\mathbf{H}} \alpha_{\mathbf{H}}^{(n-\frac{1}{2})} + \frac{\beta}{2\alpha\omega_d^2} (\alpha_{\mathbf{J}_p}^{(n-\frac{1}{2})})^T \Phi_{\mathbf{J}_p}^T \mathbb{M} \Phi_{\mathbf{J}_p} \alpha_{\mathbf{J}_p}^{(n-\frac{1}{2})} \\
&- \frac{1}{2}\Delta t (\alpha_{\mathbf{H}}^{(n-\frac{1}{2})})^T \Phi_{\mathbf{H}}^T (\mathbb{K} - \mathbb{S}^i + \mathbb{S}^e) \Phi_{\mathbf{E}} \alpha_{\mathbf{E}}^{(n)} - \frac{1}{2\alpha}\Delta t (\alpha_{\mathbf{J}_p}^{(n-\frac{1}{2})})^T \Phi_{\mathbf{J}_p}^T (-\mathbb{M}) \Phi_{\mathbf{E}} \alpha_{\mathbf{E}}^{(n)},
\end{aligned} \tag{14}$$

where the parameters α and β are defined by

$$\alpha = 1 + \frac{\gamma_d \Delta t}{2} > 1, \quad \text{and} \quad \beta = 1 - \frac{\gamma_d \Delta t}{2} < 1. \tag{15}$$

In order to make the CFL-type conditions more readable, it is assumed that

$$\frac{\gamma_d \Delta t}{2} \leq 1, \tag{16}$$

which implies

$$\frac{1}{2} \leq \frac{1}{\alpha} < 1. \tag{17}$$

Then, we have the following equalities and inequalities

$$\begin{cases}
(\alpha_{\mathbf{E}}^{(n)})^T (\Phi_{\mathbf{E}}^T \mathbb{M} \Phi_{\mathbf{E}}) \alpha_{\mathbf{E}}^{(n)} = \mathcal{I}_1^{(n)}, \\
(\alpha_{\mathbf{H}}^{(n-\frac{1}{2})})^T (\Phi_{\mathbf{H}}^T \mathbb{M} \Phi_{\mathbf{H}}) \alpha_{\mathbf{H}}^{(n-\frac{1}{2})} = \mathcal{I}_2^{(n)}, \\
(\alpha_{\mathbf{J}_p}^{(n-\frac{1}{2})})^T (\Phi_{\mathbf{J}_p}^T \mathbb{M} \Phi_{\mathbf{J}_p}) \alpha_{\mathbf{J}_p}^{(n-\frac{1}{2})} = \mathcal{I}_3^{(n)}, \\
(\alpha_{\mathbf{H}}^{(n-\frac{1}{2})})^T \Phi_{\mathbf{H}}^T (\mathbb{K} - \mathbb{S}^i + \mathbb{S}^e) \Phi_{\mathbf{E}} \alpha_{\mathbf{E}}^{(n)} \leq \mathcal{I}_4^{(n)} \\
\qquad\qquad \leq d_{N,1}^r \sqrt{\mathcal{I}_1^{(n)}} \sqrt{\mathcal{I}_2^{(n)}}, \\
(\alpha_{\mathbf{J}_p}^{(n-\frac{1}{2})})^T \Phi_{\mathbf{J}_p}^T (-\mathbb{M}) \Phi_{\mathbf{E}} \alpha_{\mathbf{E}}^{(n)} \leq \mathcal{I}_5^{(n)} \\
\qquad\qquad \leq d_{N,2}^r \sqrt{\mathcal{I}_1^{(n)}} \sqrt{\mathcal{I}_3^{(n)}},
\end{cases}$$

with

$$\begin{cases} \mathcal{I}_1^{(n)} = \|(\Phi_{\mathbf{E}}^T \mathbb{M} \Phi_{\mathbf{E}})^{\frac{1}{2}} \alpha_{\mathbf{E}}^{(n)}\|^2, \\ \mathcal{I}_2^{(n)} = \|(\Phi_{\mathbf{H}}^T \mathbb{M} \Phi_{\mathbf{H}})^{\frac{1}{2}} \alpha_{\mathbf{H}}^{(n-\frac{1}{2})}\|^2, \\ \mathcal{I}_3^{(n)} = \|(\Phi_{\mathbf{J}_p}^T \mathbb{M} \Phi_{\mathbf{J}_p})^{\frac{1}{2}} \alpha_{\mathbf{J}_p}^{(n-\frac{1}{2})}\|^2, \\ \mathcal{I}_4^{(n)} = |(\alpha_{\mathbf{H}}^{(n-\frac{1}{2})})^T (\Phi_{\mathbf{H}}^T \mathbb{M} \Phi_{\mathbf{H}})^{\frac{1}{2}} (\Phi_{\mathbf{H}}^T \mathbb{M} \Phi_{\mathbf{H}})^{-\frac{1}{2}} \\ \qquad \Phi_{\mathbf{H}}^T (\mathbb{K} - \mathbb{S}^i + \mathbb{S}^e) \Phi_{\mathbf{E}} (\Phi_{\mathbf{E}}^T \mathbb{M} \Phi_{\mathbf{E}})^{-\frac{1}{2}} (\Phi_{\mathbf{E}}^T \mathbb{M} \Phi_{\mathbf{E}})^{\frac{1}{2}} \alpha_{\mathbf{E}}^{(n)}|, \\ \mathcal{I}_5^{(n)} = |(\alpha_{\mathbf{J}_p}^{(n-\frac{1}{2})})^T (\Phi_{\mathbf{J}_p}^T \mathbb{M} \Phi_{\mathbf{J}_p})^{\frac{1}{2}} (\Phi_{\mathbf{J}_p}^T \mathbb{M} \Phi_{\mathbf{J}_p})^{-\frac{1}{2}} \\ \qquad \Phi_{\mathbf{J}_p}^T \mathbb{M} \Phi_{\mathbf{E}} (\Phi_{\mathbf{E}}^T \mathbb{M} \Phi_{\mathbf{E}})^{-\frac{1}{2}} (\Phi_{\mathbf{E}}^T \mathbb{M} \Phi_{\mathbf{E}})^{\frac{1}{2}} \alpha_{\mathbf{E}}^{(n)}|, \end{cases}$$

which might cause the lower bound of the energy to be less than optimal (and then cause the stability limit of the POD-DGTD scheme to be slightly higher). Noticing that

$$\begin{cases} \sqrt{\mathcal{I}_1^{(n)}} \sqrt{\mathcal{I}_2^{(n)}} \leq \frac{1}{2}(\mathcal{I}_1^{(n)} + \mathcal{I}_2^{(n)}), \\ \sqrt{\mathcal{I}_1^{(n)}} \sqrt{\mathcal{I}_3^{(n)}} \leq \frac{1}{2}(\mathcal{I}_1^{(n)} + \mathcal{I}_3^{(n)}), \end{cases}$$

then one can get

$$\Theta^{r,n} \geq \frac{1}{2}(\varepsilon_\infty - \frac{\Delta t d_{N,1}^r}{2} - \frac{\Delta t d_{N,2}^r}{2\alpha}) \mathcal{I}_1^{(n)} + \frac{1}{2}(1 - \frac{\Delta t d_{N,1}^r}{2}) \mathcal{I}_2^{(n)} + \frac{1}{2}(\frac{\beta}{\alpha \omega_d^2} - \frac{\Delta t d_{N,2}^r}{2\alpha}) \mathcal{I}_3^{(n)}. \quad (18)$$

Based on (17), each one of the three induced conditions is now considered separately

$$\Delta t < \frac{2\varepsilon_\infty}{d_{N,1}^r + d_{N,2}^r}, \quad \Delta t < \frac{2}{d_{N,1}^r}, \quad \text{and} \quad \Delta t < \frac{2}{\gamma_d + 2\omega_d^2 d_{N,2}^r}. \quad (19)$$

One should eventually notice that the assumption (16) is contained in the above written condition. This concludes the proof. □

Theorem 2. *Under CFL-type condition, the discrete energy $\Theta^{r,n}$ with PEC condition can be bounded in the following way*

$$\Theta^{r,n} < \frac{\Theta^{r,0}}{(\frac{1-\varrho}{1+\varrho})^n}, \quad \forall n \geq 1, \quad (20)$$

with $0 < \varrho < 1$.

Proof. Based on the definition of the discrete energy, we have

$$\begin{aligned} \Theta^{r,n+1} - \Theta^{r,n} &= \frac{1}{2}\varepsilon_\infty (\alpha_{\mathbf{E}}^{(n+1)} + \alpha_{\mathbf{E}}^{(n)})^T (\Phi_{\mathbf{E}}^T \mathbb{M} \Phi_{\mathbf{E}})(\alpha_{\mathbf{E}}^{(n+1)} - \alpha_{\mathbf{E}}^{(n)}) \\ &+ \frac{1}{2}(\alpha_{\mathbf{H}}^{(n+\frac{1}{2})})^T (\Phi_{\mathbf{H}}^T \mathbb{M} \Phi_{\mathbf{H}})(\alpha_{\mathbf{H}}^{(n+\frac{3}{2})} - \alpha_{\mathbf{H}}^{(n-\frac{1}{2})}) \\ &+ \frac{1}{2\omega_d^2}(\alpha_{\mathbf{J}_p}^{(n+\frac{1}{2})})^T (\Phi_{\mathbf{J}_p}^T \mathbb{M} \Phi_{\mathbf{J}_p})(\alpha_{\mathbf{J}_p}^{(n+\frac{3}{2})} - \alpha_{\mathbf{J}_p}^{(n-\frac{1}{2})}). \end{aligned} \quad (21)$$

We denote by $\alpha_{\mathbf{E}}^{[n+\frac{1}{2}]} = \frac{(\alpha_{\mathbf{E}}^{(n+1)} + \alpha_{\mathbf{E}}^{(n)})}{2}$. Under the CFL-type condition ($1 < \alpha < 2$, and

$0 < \beta < 1$), we have

$$\begin{aligned}
\Theta^{r,n+1} - \Theta^{r,n} &= \Delta t(\alpha_{\mathbf{E}}^{[n+\frac{1}{2}]})^T \Phi_{\mathbf{E}}^T(\mathbb{K} - \mathbb{S}^i - \mathbb{S}^h)\Phi_{\mathbf{H}}\alpha_{\mathbf{H}}^{(n+\frac{1}{2})} - \Delta t(\alpha_{\mathbf{E}}^{[n+\frac{1}{2}]})^T \Phi_{\mathbf{E}}^T \mathbb{M}\Phi_{\mathbf{J}_p}\alpha_{\mathbf{J}_p}^{(n+\frac{1}{2})} \\
&+ \Delta t(\alpha_{\mathbf{H}}^{(n+\frac{1}{2})})^T \Phi_{\mathbf{H}}^T(-\mathbb{K} + \mathbb{S}^i + \mathbb{S}^e)\Phi_{\mathbf{E}}\alpha_{\mathbf{E}}^{[n+\frac{1}{2}]} \\
&+ \frac{1}{2\omega_d^2}(\frac{\beta}{\alpha} - \frac{\alpha}{\beta})(\alpha_{\mathbf{J}_p}^{(n+\frac{1}{2})})^T(\Phi_{\mathbf{J}_p}^T \mathbb{M}\Phi_{\mathbf{J}_p})\alpha_{\mathbf{J}_p}^{(n+\frac{1}{2})} \\
&+ \frac{\Delta t}{2\alpha}(\alpha_{\mathbf{J}_p}^{(n+\frac{1}{2})})^T(\Phi_{\mathbf{J}_p}^T \mathbb{M}\Phi_{\mathbf{E}})\alpha_{\mathbf{E}}^{(n+1)} \\
&+ \frac{\Delta t}{2\beta}(\alpha_{\mathbf{J}_p}^{(n+\frac{1}{2})})^T(\Phi_{\mathbf{J}_p}^T \mathbb{M}\Phi_{\mathbf{E}})\alpha_{\mathbf{E}}^{(n)}. \qquad (22)
\end{aligned}$$

Based on the definitions of (5) and (15), we have

$$\mathbb{K} = \mathbb{K}^T,\ \mathbb{S}^i = (\mathbb{S}^i)^T,\ \mathbb{S}^h = -\mathbb{S}^e,\ (\mathbb{S}^e)^T = -\mathbb{S}^e,$$

and

$$\frac{\beta}{\alpha} - \frac{\alpha}{\beta} < 0.$$

Then, one can get

$$\Theta^{r,n+1} - \Theta^{r,n} < \underbrace{\Delta t(\frac{1-\alpha}{2\alpha})(\alpha_{\mathbf{J}_p}^{(n+\frac{1}{2})})^T(\Phi_{\mathbf{J}_p}^T \mathbb{M}\Phi_{\mathbf{E}})\alpha_{\mathbf{E}}^{(n+1)} + \Delta t(\frac{1-\beta}{2\beta})(\alpha_{\mathbf{J}_p}^{(n+\frac{1}{2})})^T(\Phi_{\mathbf{J}_p}^T \mathbb{M}\Phi_{\mathbf{E}})\alpha_{\mathbf{E}}^{(n)}}_{\zeta}. \qquad (23)$$

One can obtain the following bound for ζ

$$\begin{aligned}
|\zeta| &\leq \Delta t(\frac{\alpha-1}{2\alpha})\|\mathbb{M}^{\frac{1}{2}}\underline{\mathbf{J}}_{p,h}^{r,(n+\frac{1}{2})}\|\|\mathbb{M}^{\frac{1}{2}}\underline{\mathbf{E}}_h^{r,(n+1)}\| + \Delta t(\frac{1-\beta}{2\beta})\|\mathbb{M}^{\frac{1}{2}}\underline{\mathbf{J}}_{p,h}^{r,(n+\frac{1}{2})}\|\|\mathbb{M}^{\frac{1}{2}}\underline{\mathbf{E}}_h^{r,(n)}\| \\
&\leq \underbrace{\Delta t\frac{\omega_d}{\varepsilon_\infty}(\frac{\alpha-1}{2\alpha} + \frac{1-\beta}{2\beta})}_{\varrho}\frac{\|\mathbb{M}^{\frac{1}{2}}\underline{\mathbf{J}}_{p,h}^{r,(n+\frac{1}{2})}\|}{\omega_d}\underbrace{\max\{\varepsilon_\infty\|\mathbb{M}^{\frac{1}{2}}\underline{\mathbf{E}}_h^{r,(n+1)}\|, \varepsilon_\infty\|\mathbb{M}^{\frac{1}{2}}\underline{\mathbf{E}}_h^{r,(n)}\|\}}_{\hbar^{(n)}} \\
&\leq \frac{\varrho}{2}(\frac{\|\mathbb{M}^{\frac{1}{2}}\underline{\mathbf{J}}_{p,h}^{r,(n+\frac{1}{2})}\|^2}{\omega_d^2} + (\hbar^{(n)})^2). \qquad (24)
\end{aligned}$$

Let C be a generic constant. Under the definition of discrete energy (12) and the CFL-type condition, we have

$$\frac{\|\mathbb{M}^{\frac{1}{2}}\underline{\mathbf{J}}_{p,h}^{r,(n+\frac{1}{2})}\|^2}{\omega_d^2} \leq C\Theta^{r,n+1}, \quad (\hbar^{(n)})^2 \leq C(\Theta^{r,n+1} + \Theta^{r,n}).$$

This yields

$$\Theta^{r,n+1} - \Theta^{r,n} \leq \varrho\Theta^{r,n+1} + \frac{\varrho}{2}\Theta^{r,n},$$

which leads to

$$\Theta^{r,n+1} \leq \frac{1+\frac{\varrho}{2}}{1-\varrho}\Theta^{r,n} < \frac{1+\varrho}{1-\varrho}\Theta^{r,n},$$

with $\varrho > 0$. It is also required that $\varrho < 1$, which can be proved to be equivalent to

$$\Delta t < \frac{2}{\sqrt{\gamma_d^2 + 2\frac{\gamma_d\omega_d}{\varepsilon_\infty}}}.$$

In particular, the condition can be shown to be less restrictive than the $\Delta t \leq \frac{2}{\gamma_d}$. This completes the proof. □

4. Numerical experiments

In this section, numerical examples for the 3-D time-domain Maxwell's equations with Drude model are given. First, we present the problem of the standing wave in a cubic PEC cavity for which a simple analytical solution can be computed, to validate the implementation of the POD-DGTD method. We then consider the problem of the scattering of a plane wave by a gold nanosphere to investigate the behavior of the method for optical problems. Finally, a more challenging application is considered in the form of the scattering of a plane wave by a plasmonic bowtie nanoantenna. All DGTD and POD-DGTD methods with the LF_2 time scheme have been implemented in MATLAB. All our tests are performed on a workstation equipped with an Intel Xeon CPU running at 3.70 GHz with 32 GB of RAM memory. The values of the CFL number of POD-DGTD method corresponds to the numerical stability. We choose $\rho = 10^{-4}$ to compute the dimension $k_{\mathbf{u}}$ ($\mathbf{u} \in \{\mathbf{E}, \mathbf{H}, \mathbf{J}_p\}$) of the POD basis in all experiments.

4.1. Standing wave in a cubic PEC cavity

We first consider the propagation of the (1,1,1) mode in a PEC cubic cavity $\Omega_\square = [0, L]^3$ [51]. An artificial current source $\mathbf{J}_s$ is added to the second equation of (2) such that the analytical solution coincides with the time-domain Maxwell-Drude equations

$$\begin{cases} \partial_t \mathbf{H} & + & \text{curl}\mathbf{E} = 0, \\ \varepsilon_\infty \partial_t \mathbf{E} & - & \text{curl}\mathbf{H} + \mathbf{J}_p = \mathbf{J}_s, \\ \partial_t \mathbf{J}_p & + & \gamma_d \mathbf{J}_p - \omega_d^2 \mathbf{E} = 0, \end{cases} \tag{25}$$

where the artificial current source $\mathbf{J}_s$ is defined as

$$\mathbf{J}_s = \begin{pmatrix} (\xi \sin(x_t t) - \vartheta \gamma_d \cos(x_t t)) \cos(x_m x) \sin(x_m y) \sin(x_m z) \\ 0 \\ (-\xi \sin(x_t t) + \vartheta \gamma_d \cos(x_t t)) \sin(x_m x) \sin(x_m y) \cos(x_m z) \end{pmatrix}.$$

Here, $x_m = \dfrac{\pi}{L}$, which is deduced from the PEC boundary condition; $x_t = \dfrac{\pi\sqrt{3}}{L}$, which determines the angular frequency of the time evolution. As we are only considering the (1,1,1) mode, the signal frequency is given by $f = \dfrac{\sqrt{3}c_0}{2L}$ with c_0 being the wave speed in vacuum. The coefficients ϑ and ξ are defined as

$$\begin{cases} \vartheta = \dfrac{\omega_d^2}{x_t^2 + \gamma_d^2}, \\ \xi = \varepsilon_\infty x_t - 3\dfrac{x_m^2}{x_t} - \vartheta x_t. \end{cases}$$

For the Drude parameters, we choose $\varepsilon_\infty = 3.7362$, $\omega_d = 1.3871 \times 10^7$ GHz, $\gamma_d = 4.41544 \times 10^4$ GHz in this study. For detailed descriptions of the exact soulution of (25) with the current source see [51].

We present the results for the signal frequency $f = 3 \times 10^5$ GHz. The characteristic simulations are performed on an unstructured mesh with 10,029 nodes, 49,984 elements, and mesh size $h = 9.668 \times 10^{-9}$ m. The total simulation time is set to $T_f = 6.67$ fs which corresponds to two temporal periods. As a general rule, keeping the number of snapshots ℓ small allows to minimize the computational cost in offline stage. So, we first investigate the effect of the

parameter ℓ on the accuracy of POD-based ROM. Figure 1 shows the total L^2 error between the DGTD and POD-DGTD solutions, in logarithmic scale, in which the L^2 error is defined by

$$\max_n(\varepsilon_\infty\|\underline{\mathbf{E}}_h^{(n)}-\underline{\mathbf{E}}_h^{r,(n)}\|_{L^2(\Omega)}^2+\|\underline{\mathbf{H}}_h^{(n)}-\underline{\mathbf{H}}_h^{r,(n)}\|_{L^2(\Omega)}^2+\frac{1}{\omega_d^2}\|\underline{\mathbf{J}}_{p,h}^{(n)}-\underline{\mathbf{J}}_{p,h}^{r,(n)}\|_{L^2(\Omega)}^2)^{\frac{1}{2}}. \tag{26}$$

Moreover, we also show the CPU time T_{POD} for the construction of the POD basis. We only apply the DGTD methods with $\mathbb{P}_1$ and $\mathbb{P}_2$ approximation (because the theoretical error of the centered flux-based DGTD method with LF_2 time scheme behaves as $\mathcal{O}(\Delta t^2+h^p)$ [13, 19]). Besides, we find that the maximum time step size $\Delta t_{\text{POD-DGTD}}$ is larger than the maximum time step size Δt_{DGTD} with the LF_2 time scheme by computing (7) and (13). Hence, in order to calculate the error, the time step size $\Delta t_{\text{POD-DGTD}}$ of the POD-based ROM is set to the same value as that of the time step size Δt_{DGTD} of the DGTD scheme.

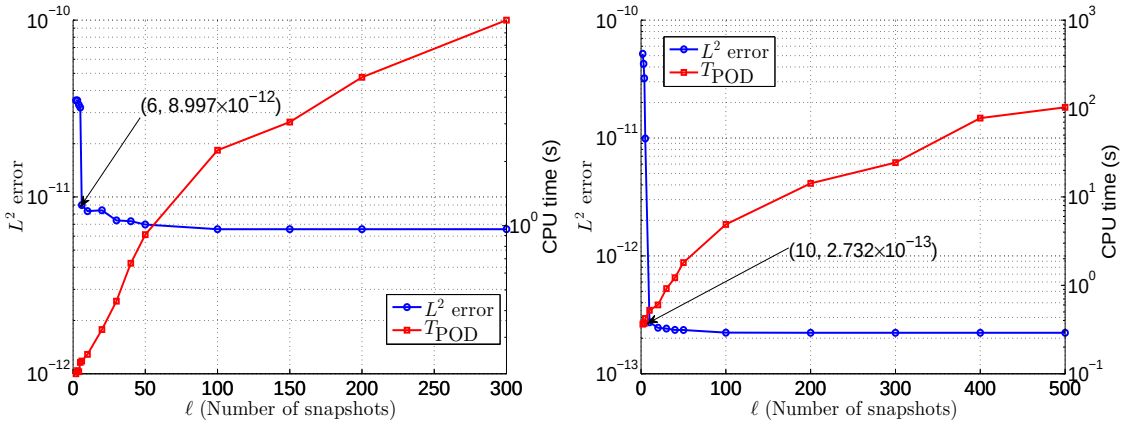

Figure 1: Standing wave in a cubic PEC cavity: L^2 error between the DGTD and POD-DGTD solutions and CPU time versus the number of snapshots ℓ with (a) $\mathbb{P}_1$ and (b) $\mathbb{P}_2$ approximation.

It is easily observed that the L^2 error is rapidly decreasing and stabilizes to a limit value while T_{POD} is increasing when increasing the number of snapshots ℓ. In particular, one can find that it is unnecessary to extract offline the total transient solutions at each time step as snapshots from Figure 1. So, we can respectively take $\ell=6$ and 10 equidistantly distributed snapshot vectors for the POD-DGTD method with $\mathbb{P}_1$ and $\mathbb{P}_2$ approximation, where the number of snapshots ℓ is about $N_t^{1/3}$. Figure 2 shows the time evolution of the total L^2 error between the POD-based MOR and DGTD scheme with the number of snapshots ℓ being 6 and 10 for $\mathbb{P}_1$ and $\mathbb{P}_2$ approximation, respectively.

The exact and numerical solutions calculated by the DGTD and POD-DGTD methods with $\mathbb{P}_2$ approximation at selected locations in the parallelepiped are shown in Figure 3. We see that the POD-DGTD solutions coincide with the DGTD and analytical solutions. This confirms that the POD-based ROM is accurate.

We then compare the computational performance of the POD-DGTD and DGTD methods in Table 1, in which the CPU time denotes the time loop by using the DGTD or POD-DGTD method with LF_2 time scheme (online stage).

In Table 1, we observe that the POD-DGTD method significantly reduces the required number of time iterations to reach the final physical time T_f due of the increase of the acceptable time step size. More precisely, we find that for the POD-DGTD method, the time step size $\Delta t_{\text{POD-DGTD}}$ is respectively about 19 and 44 times larger than that of the DGTD method with $\mathbb{P}_1$ and $\mathbb{P}_2$ approximation. Besides, we can observe that the POD-DGTD method is much

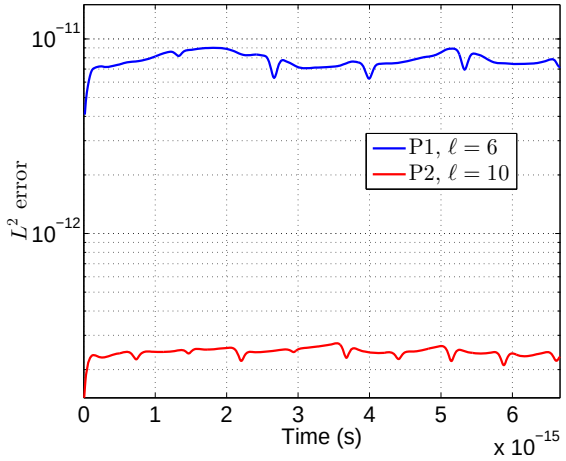

Figure 2: Standing wave in a cubic PEC cavity: time evolution of the total L^2 error obtained by the POD-DGTD method.

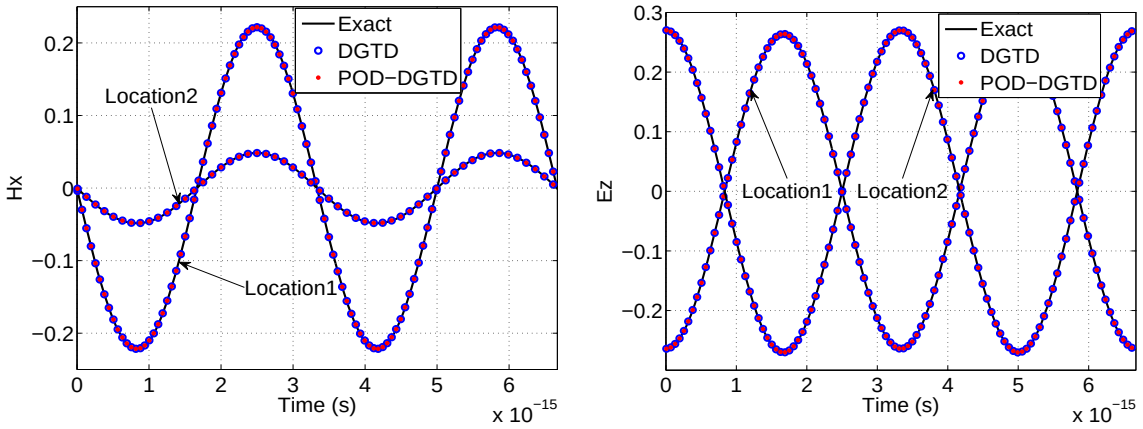

(a) (b)

Figure 3: Standing wave in a cubic PEC cavity: time evolution of the fields (a) H_x and (b) E_z at the locations with coordinates (7×10^{-7} m, 7×10^{-7} m, and 7×10^{-7} m) (Location1) and (3.5×10^{-7} m, 3.5×10^{-7} m, and 3.5×10^{-7} m) (Location2), obtained by the POD-DGTD method with $\mathbb{P}_2$ approximation.

Table 1: Standing wave in a cubic PEC cavity: critical time step size and CPU time for the DGTD and POD-DGTD methods, with $\mathbb{P}_k$ approximation ($k = 1, 2$).

$\mathbb{P}_k$	Method	DoF	Δt (m)	CPU time (s)	$\frac{\Delta t_{\text{POD-DGTD}}}{\Delta t_{\text{DGTD}}}$	$\frac{\text{CPU}_{\text{DGTD}}}{\text{CPU}_{\text{POD-DGTD}}}$
$\mathbb{P}_1$	DGTD	1,799,424	4.298×10^{-9}	87	19	218
	POD-DGTD	15	8.166×10^{-8}	0.4		
$\mathbb{P}_2$	DGTD	4,498,560	1.869×10^{-9}	921	44	419
	POD-DGTD	25	8.222×10^{-8}	2.2		

faster than the DGTD method, which yields 218 and 419 speedups for $\mathbb{P}_1$ to $\mathbb{P}_2$ approximation, respectively. From Figure 1 and Table 1, we can find that the POD-DGTD method can save the required CPU time while maintaining an acceptable level of accuracy.

4.2. Near-field resonance of a gold nanosphere

We now consider the simulation of the near-field, sub-wavelength resonance of a single gold nanosphere lying in vacuum under a plane wave excitation, which can strongly enhance the electric field due to the phenomenon of surface plasmon resonance [57]. The radius of the nanosphere r is taken to be 20 nm. The computational domain is artificially truncated by a 200 nm diameter sphere on which the first order Silver-Müller ABC is applied. The sphere is illuminated with a sinusoidal plane wave propagating in the z direction, which the amplitude is modulated in time with a gaussian profile. The source is set as an incident plane wave polarized on the x component. The incident field is then defined as

$$E_x^{\text{inc}} = \mathbf{A}_0 \sin(2\pi f_c(t - 4\tau - \mathbf{k}(\mathbf{x} - \mathbf{x}_0)/c_0)) e^{-\frac{(t-4\tau)^2}{\tau^2}},$$

where $\mathbf{A}_0 = (1, 0, 0)$, $\mathbf{k} = (0, 0, 1)$, $\mathbf{x}_0 = (0, 0, 0)$, and $\mathbf{x} = (x, y, z)$; f_c is the central frequency of the sinusoidal modulated Gaussian pulse, and τ represents its broadening. One can get H_y^{inc} based on the first equation of (2). The permittivity of the gold nanosphere [12] is considered to follow the Drude model, and the parameters are summed up in Table 2. The mesh used for the simulation is shown in Figure 4. It consists of 45,536 vertices and 266,559 tetrahedra of which 42,102 tetrahedra are located inside the gold nanosphere, where the minimal and maximum mesh edge length is 7.626×10^{-10} m and 1.322×10^{-8} m, respectively. The physical simulation time is fixed to $T_f = 20$ fs. In this case, the number of snapshots ℓ is taken 37 and 48 ($\ell = N_t^{1/3}$) for $\mathbb{P}_1$ and $\mathbb{P}_2$ approximation, respectively.

Table 2: Parameters set for the gold nanosphere.

ε_∞	ω_d (Thz)	γ_d (Thz)	f_c (Thz)	τ (fs)
1	1.19×10^4	141	576.92	2

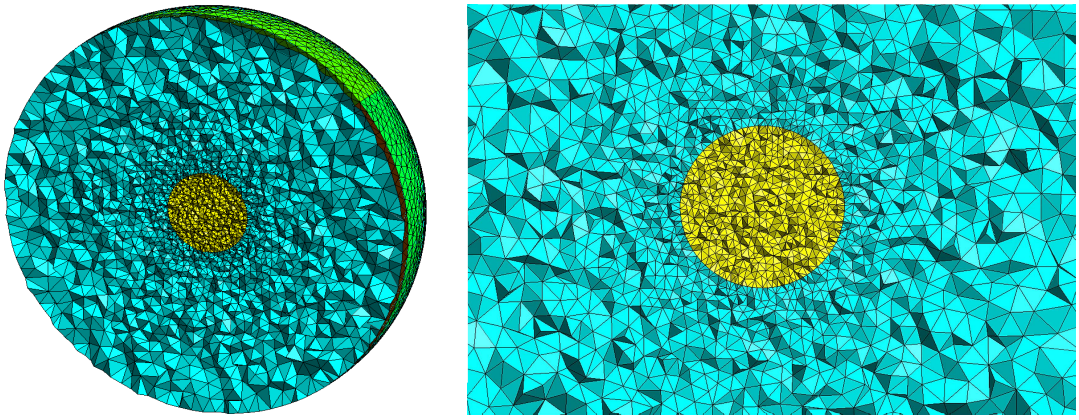

Figure 4: Partial views of the tetrahedral meshes used for the simulation of the scattering of a plane wave by a single nanosphere.

The numerical solutions obtained with the POD-based ROM are compared with those resulting from the DGTD scheme with $\mathbb{P}_k$ approximation ($k = 1, 2$) to verify the accuracy of the

POD-DGTD method. The time evolution of the fields E_x and H_y at selected points in the domain for the DGTD and POD-DGTD methods is shown in Figure 5.

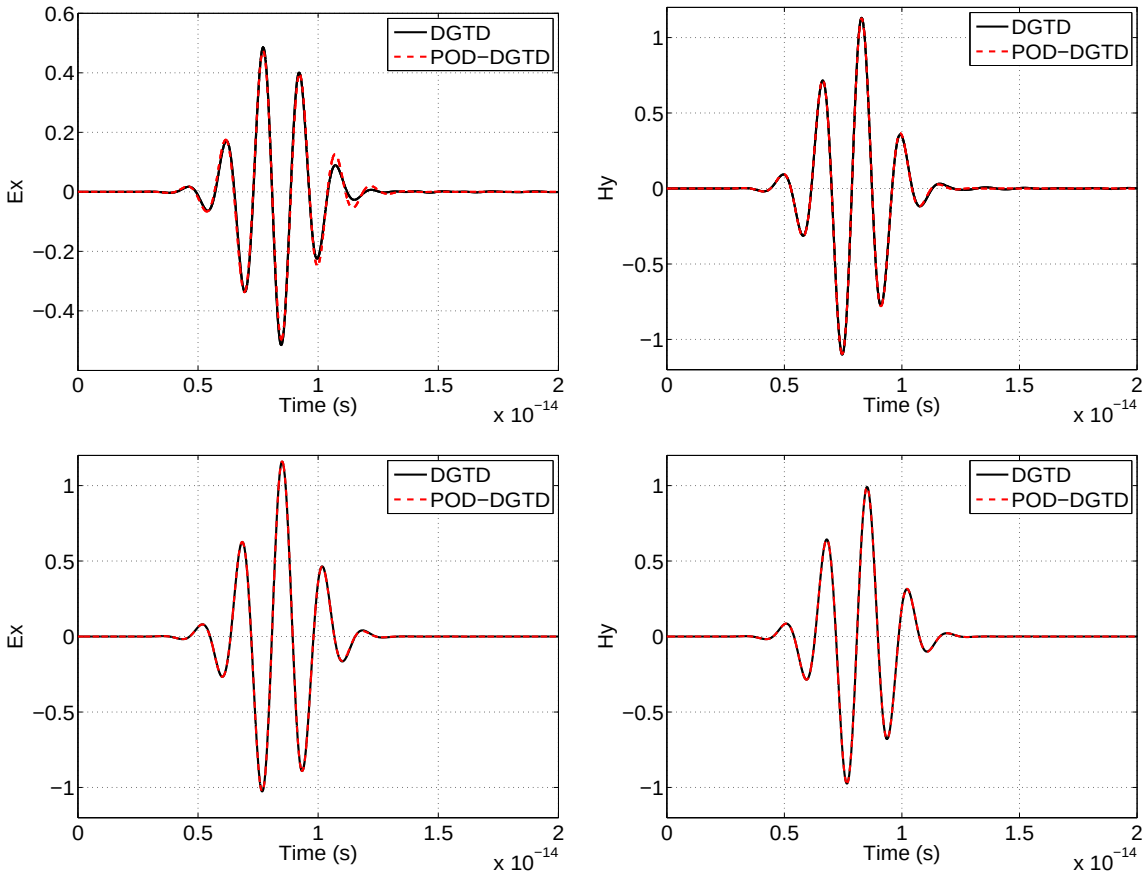

Figure 5: Scattering of a plane wave by a single nanosphere: time evolution of the fields E_x (left) and H_y (right) at the locations with coordinates (1.6×10^{-8} m, -5.7×10^{-9} m, and 1.9×10^{-9} m) and (-4.6×10^{-8} m, -7.4×10^{-9} m, and 2.3×10^{-8} m), obtained by the POD-DGTD method with $\mathbb{P}_1$ (top) and $\mathbb{P}_2$ (bottom) approximation, respectively.

We find that the numerical solutions obtained by the DGTD and POD-DGTD methods with $\mathbb{P}_2$ approximation agree very well. Figure 6 shows the distributions of the modulus of the electric field in the Fourier domain at the source central frequency f_c with $\mathbb{P}_2$ approximation. A more precise analysis of the results is displayed in Figure 7 which represents the evolution of the modulus of the electric field along the x axis.

Combining Figures 6 and 7, one can in particular notice an enhanced field at the poles of the sphere. The time evolution of the total L^2 error between the POD-based MOR and DGTD scheme, with the number of snapshots ℓ being 37 and 48 for $\mathbb{P}_1$ and $\mathbb{P}_2$ approximation respectively, is given in Figure 8.

One can see that the POD-based ROM is stable. From this experiment, we can find that the POD-DGTD method is effective for a broadband application.

We further investigate the efficiency of the POD-based ROM. The results are summarized in Table 3. From Table 3 and Figures 5, 6, and 7, we can find that the POD-based ROM can reduce the problem size by several orders of magnitude without compromising the accuracy of solution. Besides, the critical time step size of POD-DGTD method is 35, and 45 times larger than that of the DGTD method with $\mathbb{P}_1$ and $\mathbb{P}_2$ approximation, respectively. The DGTD method with $\mathbb{P}_1$ approximation takes 17 h 43 mn to complete the entire simulation. In contrast,

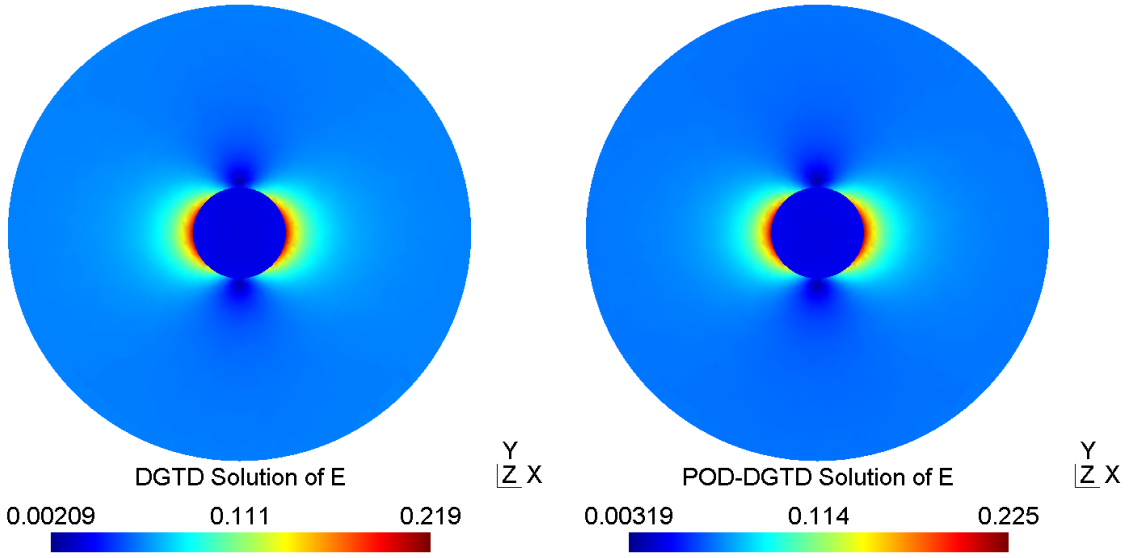

Figure 6: Scattering of a plane wave by a single nanosphere: module of the electric field in the Fourier domain at the source central frequency f_c obtained by the DGTD (left) and POD-DGTD (right) methods at the plane XOY.

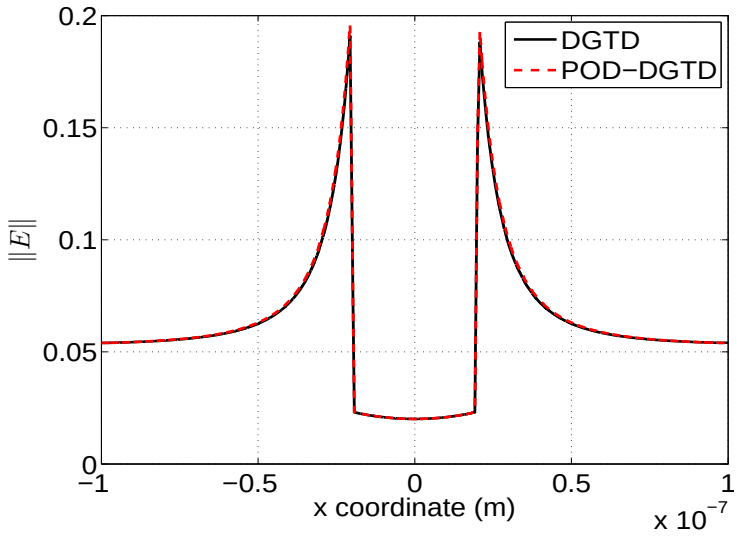

Figure 7: Scattering of a plane wave by a single nanosphere: 1-D distribution along the x axis of the modulus of the POD-DGTD and DGTD solutions of the electric field with $\mathbb{P}_2$ approximation.

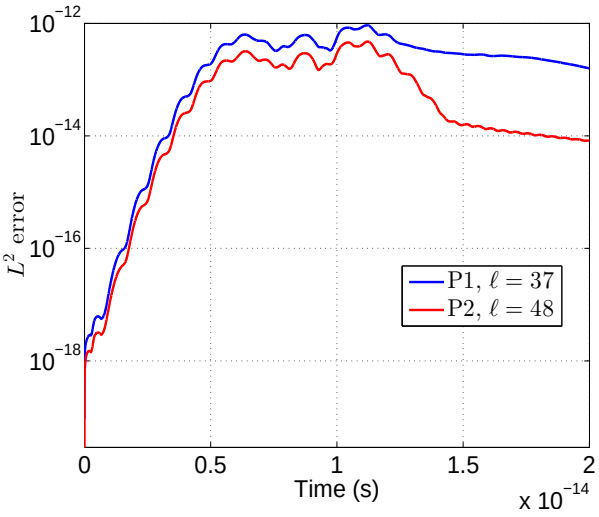

Figure 8: Scattering of a plane wave by a single nanosphere: time evolution of the total L^2 error obtained by the POD-DGTD method.

the POD-DGTD method only requires 10 mn, which is 106 times faster than the DGTD method. Similarly, the DGTD method with $\mathbb{P}_2$ approximation yields a 300 speedup.

Table 3: Scattering of a plane wave by a single nanosphere: critical time step size and CPU time for the DGTD and POD-DGTD methods, with $\mathbb{P}_k$ approximation ($k = 1, 2$).

$\mathbb{P}_k$	Method	DoF	Δt (m)	CPU time	$\frac{\Delta t_{\text{POD-DGTD}}}{\Delta t_{\text{DGTD}}}$	$\frac{\text{CPU}_{\text{DGTD}}}{\text{CPU}_{\text{POD-DGTD}}}$
$\mathbb{P}_1$	DGTD	6,902,640	1.463×10^{-10}	17 h 43 mn	35	106
	POD-DGTD	97	5.120×10^{-9}	10 mn		
$\mathbb{P}_2$	DGTD	17,256,600	6.501×10^{-11}	154 h 46 mn	45	300
	POD-DGTD	64	2.925×10^{-9}	31 mn		

4.3. Bowtie nanoantenna

To further illustrate the benefits of the POD-based ROM, the simulation of the scattering of a plane wave by a gold bowtie nanoantenna (dimer nanoprisms) is finally presented. This structure can strongly enhance the electric field between the tips of the two triangular nanoparticles for longitudinal polarization (see Figure 9) [58]. The gold bowtie nanoantenna is composed of a pair of equilateral prisms, with a thickness of 10 nm, edge length of 100 nm and a spacing gap of 3 nm inspired by [19] in vacuum. Additionally, the actual geometry of the antenna includes small roundings at the edges and tips. In this case, the rounding radius r is 2 nm, and is uniform for all edges and tips.

The permittivity of gold bowtie nanoantenna is given by the Drude model, which is the same as the standing wave in the cubic PEC cavity presented in Section 4.1. The computational domain is artificially truncated by a parallelepiped with 400 nm side length on which the first order Silver-Müller ABC is imposed. The gold bowtie nanoantenna is also illuminated with a sinusoidal plane wave propagating in the z direction, which the amplitude is modulated in time with a gaussian profile. The source is set as an incident plane wave polarized along the major

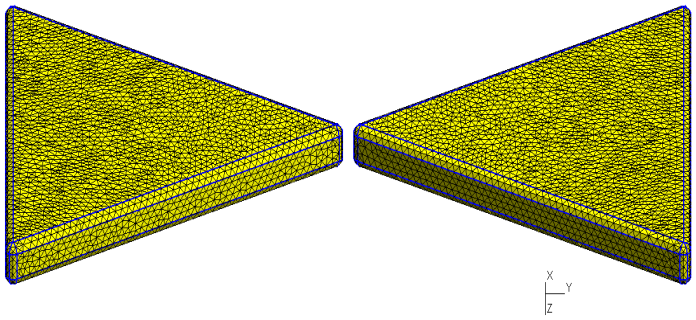

Figure 9: Bowtie nanoantenna with rounded edges.

axis of the bowtie nanoantenna (here, the y component). The incident field is then defined as

$$E_y^{\text{inc}} = \mathbf{A}_0 \sin(2\pi f_c(t - 4\tau - \mathbf{k}(\mathbf{x} - \mathbf{x}_0)/c_0))e^{-\frac{(t-4\tau)^2}{\tau^2}},$$

where $\mathbf{A}_0$, $\mathbf{k}$, $\mathbf{x}_0$, and $\mathbf{x}$ are like as in Section 4.2, the central frequency f_c is 500 THz, and the broadening τ is 3 fs. Similarly, one can get H_x^{inc} based on the first equation of (2). The mesh, which is generated by Gmsh, is partially visualized on Figure 10.

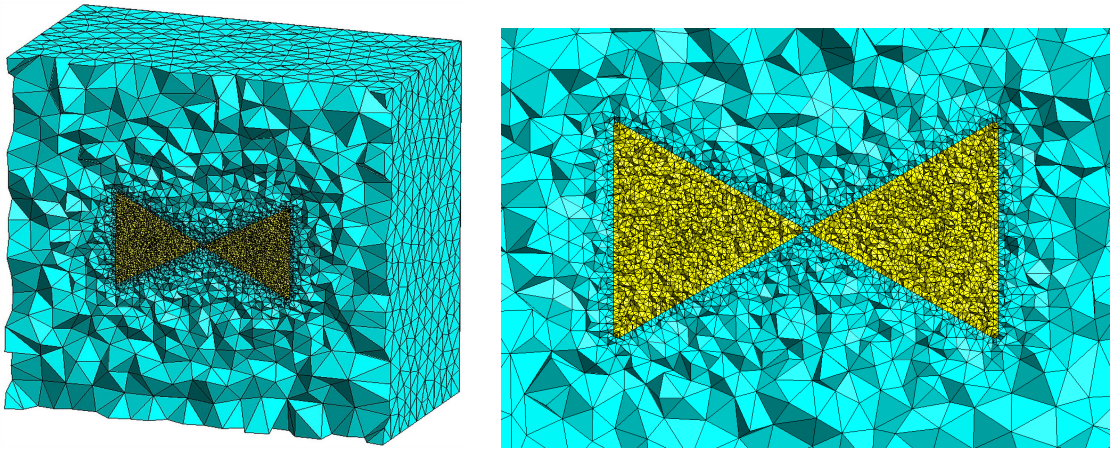

Figure 10: Partial views of the tetrahedral meshes used for the simulation of the scattering of a plane wave by a gold bowtie nanoantenna.

The underlying tetrahedral mesh consists of 31,951 vertices and 189,246 tetrahedra, where the minimal and maximum mesh edge length is 7.294×10^{-10} m and 5.512×10^{-8} m, respectively. The total simulation time T_f is set to 20 fs. In this case, the number of snapshots ℓ is taken 37 and 48 ($\ell = N_t^{1/3}$) for $\mathbb{P}_1$ and $\mathbb{P}_2$ approximation, respectively.

The contour lines of the modules of the Fourier transform of the electric field at the central frequency f_c obtained by the DGTD and POD-DGTD methods with $\mathbb{P}_2$ approximation in the YOX and YOZ planes are shown in Figure 11.

In additional, a 1-D cut along the y axis difference between the DGTD and the POD-DGTD solutions with $\mathbb{P}_2$ approximation is represented in Figure 12.

We observe that the numerical solutions obtained by DGTD and POD-DGTD methods agree very well. In Figure 13, we plot the time evolution of the total L^2 error between the POD-based MOR and DGTD scheme, with the number of snapshots ℓ being 37 and 48 for $\mathbb{P}_1$ and $\mathbb{P}_2$ approximation, respectively.

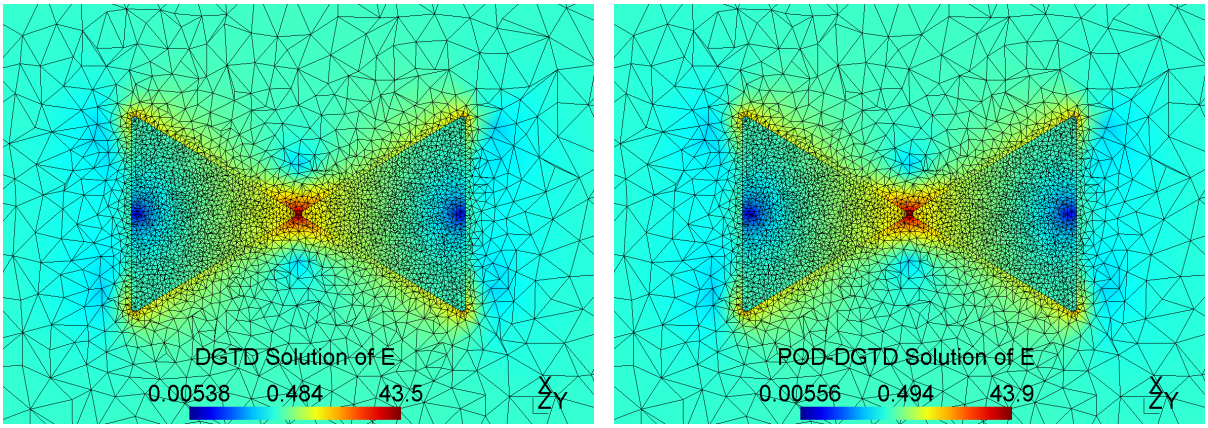

(a) DGTD, YOX (b) POD-DGTD, YOX

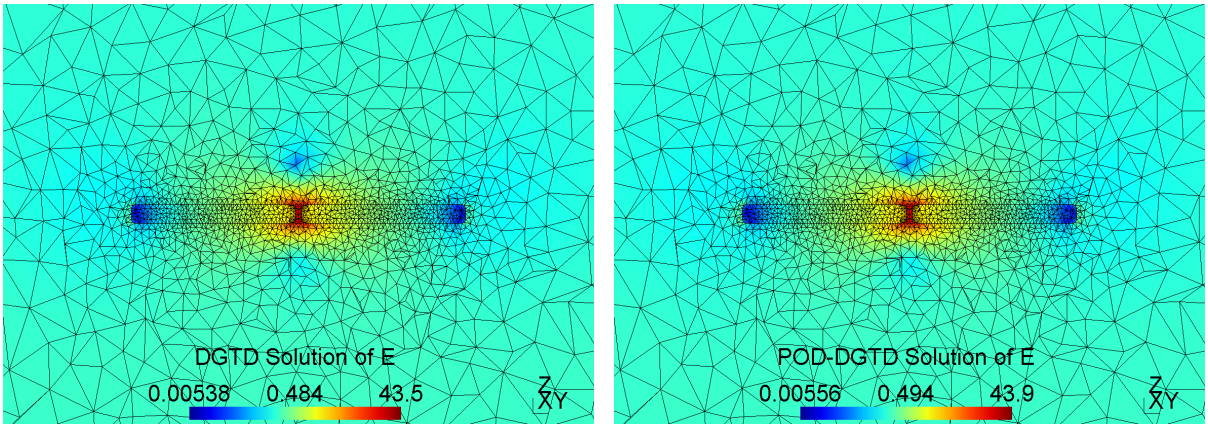

(c) DGTD, YOZ (d) POD-DGTD, YOZ

Figure 11: Scattering of a plane wave by a gold bowtie nanoantenna: module of the electric field in the Fourier domain at the source central frequency f_c obtained by the DGTD (left) and POD-DGTD (right) methods at the planes YOX (top) and YOZ (bottom).

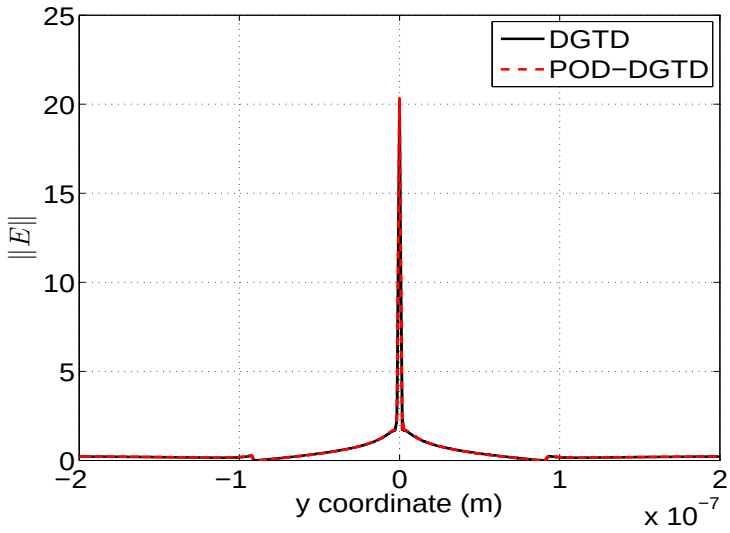

Figure 12: Scattering of a plane wave by a gold bowtie nanoantenna: 1-D distribution along the y axis of the modulus of the POD-DGTD and DGTD solutions of the electric field with $\mathbb{P}_2$ approximation.

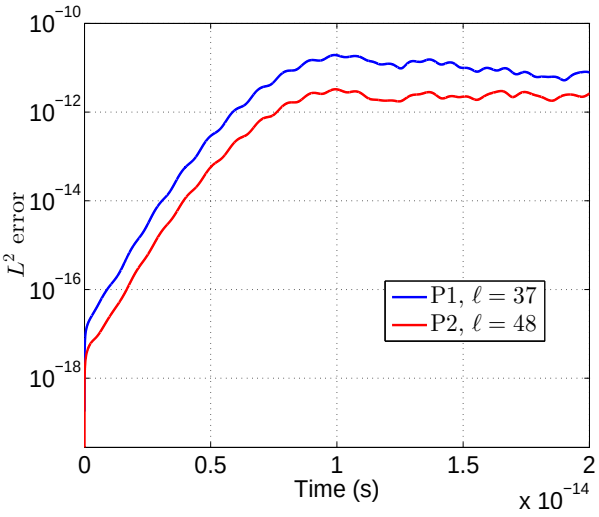

Figure 13: Scattering of a plane wave by a gold bowtie nanoantenna: time evolution of the total L^2 error obtained by the POD-DGTD method.

The performance results obtained by the DGTD and POD-DGTD methods with $\mathbb{P}_k$ ($k = 1, 2$) approximation are summarized in Table 4.

Table 4: Scattering of a plane wave by a gold bowtie nanoantenna: critical time step size and CPU time for the DGTD and POD-DGTD methods, with $\mathbb{P}_k$ approximation ($k = 1, 2$).

$\mathbb{P}_k$	Method	DoF	Δt (m)	CPU time (h)	$\frac{\Delta t_{\text{POD-DGTD}}}{\Delta t_{\text{DGTD}}}$	$\frac{\text{CPU}_{\text{DGTD}}}{\text{CPU}_{\text{POD-DGTD}}}$
$\mathbb{P}_1$	DGTD	5,227,872	1.175×10^{-10}	14 h 41 mn	40	176
	POD-DGTD	73	4.700×10^{-9}	5 mn		
$\mathbb{P}_2$	DGTD	13,069,680	5.222×10^{-11}	132 h 8 mn	50	378
	POD-DGTD	63	2.611×10^{-9}	21 mn		

Note that the critical time step size of POD-DGTD method is 40, and 50 times larger than that of the DGTD method with $\mathbb{P}_1$ and $\mathbb{P}_2$ approximation, respectively. In addition, we find that the DGTD method with $\mathbb{P}_1$ and $\mathbb{P}_2$ approximation spend 14 h 41 mn and 132 h 8 mn, while the POD-DGTD method only spend 5 mn and 21 mn, respectively.

5. Conclusion

In this paper, we have proposed a POD-based ROM (Galerkin projection) in combination with a high order DGTD method for the numerical simulation of 3-D Maxwell's equations with the Drude dispersive model. Snapshot vectors in this work are chosen from the high fidelity DGTD method with an explicit LF_2 scheme for the integration time. In this study, the same scheme has been applied to the semi-discrete POD-based scheme, however, other options, such as the implicit Crank-Nicolson scheme, could be used. The stability of the ROM with LF_2 time scheme has been analyzed through an energy approach. Numerical experiment for 3-D nanophotonic problems have allowed us to demonstrate that the ROM can reduce the computational time while preserving an acceptable level of accuracy. Therefore, POD-Galerkin reduced-order DGTD method is a promising in the field of optical and electronic engineering.

In the near future, we will consider the numerical simulation of more general physical optical models (non-local model [8, 9]), and the possibly adaptive selection strategies for choosing the snapshots.

Acknowledgments

The authors are very grateful for the constructive advices from anonymous reviewers and the help of the editors.

Declarations

Fundings

The first author is supported by the NSFC (Grant No. 12101511). The second author is supported by the NSFC (Grant No. 61772003) and the Key Projects of Applied Basic Research in Sichuan Province (Grant No. 2020YJ0216).

Conflicts of interest/Competing interests

We declare that we have no financial and personal relationships with other people or organizations that can inappropriately influence our work, there is no professional or other personal interest of any nature or kind in any product, service and/or company that could be construed as influencing the position presented in, or the review of, the manuscript entitled.

Availability of data and material

Not applicable

Code availability

Not applicable

References

[1] S. A. Maier, Plasmonics: fundamentals and applications, Springer Science & Business Media, 2007.

[2] F. Vidal-Codina, N.-C. Nguyen, J. Peraire, Computing parametrized solutions for plasmonic nanogap structures, Journal of Computational Physics 366 (2018) 89–106.

[3] M. Zapata Herrra, Plasmon resonances and tunneling in sub-nanometric systems, Ph.D. thesis, Universidad de los Andes (2015).

[4] L. Li, S. Lanteri, N. A. Mortensen, M. Wubs, A hybridizable discontinuous Galerkin method for solving nonlocal optical response models, Computer Physics Communications 219 (2017) 99–107.

[5] J. Li, Y. Huang, Time-domain finite element methods for Maxwell's equations in metamaterials, Springer Science & Business Media, 2012.

[6] P. Drude, Zur elektronentheorie der metalle, Annalen der Physik 306 (3) (1900) 566–613.

[7] M. Dressel, M. Scheffler, Verifying the Drude response, Annalen der Physik 15 (7-8) (2006) 535–544.

[8] S. Raza, S. I. Bozhevolnyi, M. Wubs, N. A. Mortensen, Nonlocal optical response in metallic nanostructures, Journal of Physics: Condensed Matter 27 (18) (2015) 183204. doi:https://doi.org/10.1088/0953-8984/27/18/183204.

[9] N. A. Mortensen, S. Raza, M. Wubs, T. Søndergaard, S. I. Bozhevolnyi, A generalized non-local optical response theory for plasmonic nanostructures, Nature Communications 5 (2014) 3809. doi:https://doi.org/10.1038/ncomms4809.

[10] K. Yee, Numerical solution of initial boundary value problems involving Maxwell's equations in isotropic media, IEEE Transactions on Antennas and Propagation 14 (3) (1966) 302–307.

[11] F. Vidal-Codina, N.-C. Nguyen, S.-H. Oh, J. Peraire, A hybridizable discontinuous Galerkin method for computing nonlocal electromagnetic effects in three-dimensional metallic nanostructures, Journal of Computational Physics 355 (2018) 548–565.

[12] R. Léger, J. Viquerat, C. Durochat, C. Scheid, S. Lanteri, A parallel non-conforming multi-element DGTD method for the simulation of electromagnetic wave interaction with metallic nanoparticles, Journal of Computational and Applied Mathematics 270 (2014) 330–342.

[13] J. S. Hesthaven, T. Warburton, Nodal discontinuous Galerkin methods: algorithms, analysis, and applications, Springer Science & Business Media, 2007.

[14] S. Dosopoulos, B. Zhao, J.-F. Lee, Non-conformal and parallel discontinuous Galerkin time domain method for Maxwell's equations: EM analysis of IC packages, Journal of Computational Physics 238 (2013) 48–70.

[15] J. Viquerat, S. Lanteri, Simulation of near-field plasmonic interactions with a local approximation order discontinuous Galerkin time-domain method, Photonics and Nanostructures-Fundamentals and Applications 18 (2016) 43–58.

[16] M. Bernacki, L. Fezoui, S. Lanteri, S. Piperno, Parallel discontinuous Galerkin unstructured mesh solvers for the calculation of three-dimensional wave propagation problems, Applied Mathematical Modelling 30 (8) (2006) 744–763.

[17] K. Stannigel, M. König, J. Niegemann, K. Busch, Discontinuous Galerkin time-domain computations of metallic nanostructures, Optics Express 17 (17) (2009) 14934–14947.

[18] K. Busch, M. König, J. Niegemann, Discontinuous Galerkin methods in nanophotonics, Laser & Photonics Reviews 5 (6) (2011) 773–809.

[19] J. Viquerat, Simulation of electromagnetic waves propagation in nano-optics with a high-order discontinuous Galerkin time-domain method, Ph.D. thesis, INRIA (2015).

[20] N. Schmitt, C. Scheid, S. Lanteri, A. Moreau, J. Viquerat, A DGTD method for the numerical modeling of the interaction of light with nanometer scale metallic structures taking into account non-local dispersion effects, Journal of Computational Physics 316 (2016) 396–415.

[21] S. Lanteri, C. Scheid, J. Viquerat, Analysis of a generalized dispersive model coupled to a DGTD method with application to nanophotonics, SIAM Journal on Scientific Computing 39 (3) (2017) A831–A859.

[22] N. Schmitt, C. Scheid, J. Viquerat, S. Lanteri, Simulation of three-dimensional nanoscale light interaction with spatially dispersive metals using a high order curvilinear DGTD method, Journal of Computational Physics 373 (2018) 210–229.

[23] M. Lyu, W. C. Chew, L. Jiang, M. Li, L. Xu, Numerical simulation of a coupled system of Maxwell equations and a gas dynamic model, Journal of Computational Physics 409 (2020) 109354. doi:https://doi.org/10.1016/j.jcp.2020.109354.

[24] S. Nicaise, C. Scheid, Stability and asymptotic properties of a linearized hydrodynamic medium model for dispersive media in nanophotonics, Computers & Mathematics with Applications 79 (12) (2020) 3462–3494.

[25] L. Li, S. Lanteri, R. Perrussel, A hybridizable discontinuous Galerkin method combined to a Schwarz algorithm for the solution of 3-D time-harmonic Maxwell's equation, Journal of Computational Physics 256 (2014) 563–581.

[26] K. Li, T.-Z. Huang, L. Li, S. Lanteri, A reduced-order DG formulation based on POD method for the time-domain Maxwell's equations in dispersive media, Journal of Computational and Applied Mathematics 336 (2018) 249–266.

[27] B. Peherstorfer, K. Willcox, M. Gunzburger, Survey of multifidelity methods in uncertainty propagation, inference, and optimization, SIAM Review 60 (3) (2018) 550–591.

[28] K. Li, T.-Z. Huang, L. Li, S. Lanteri, Non-intrusive reduced-order modeling of parameterized electromagnetic scattering problems using cubic spline interpolation, Journal of Scientific Computing 87 (2) (2021). doi:doi:https://doi.org/10.1007/s10915-021-01467-2.

[29] P. Benner, S. Gugercin, K. Willcox, A survey of projection-based model reduction methods for parametric dynamical systems, SIAM Review 57 (4) (2015) 483–531.

[30] K. Kunisch, S. Volkwein, Optimal snapshot location for computing POD basis functions, ESAIM: Mathematical Modelling and Numerical Analysis 44 (3) (2010) 509–529.

[31] Q. Wang, N. Ripamonti, J. S. Hesthaven, Recurrent neural network closure of parametric POD-Galerkin reduced-order models based on the Mori-Zwanzig formalism, Journal of Computational Physics 410 (2020) 109402. doi:https://doi.org/10.1016/j.jcp.2020.109402.

[32] P. Phalippou, S. Bouabdallah, P. Breitkopf, P. Villon, M. Zarroug, 'on-the-fly' snapshots selection for proper orthogonal decomposition with application to nonlinear dynamics, Computer Methods in Applied Mechanics and Engineering 367 (2020) 113120. doi:https://doi.org/10.1016/j.cma.2020.113120.

[33] L. Sirovich, Turbulence and the dynamics of coherent structures. I. Coherent structures, Quarterly of Applied Mathematics 45 (3) (1987) 561–571.

[34] L. Grinberg, Proper orthogonal decomposition of atomistic flow simulations, Journal of Computational Physics 231 (16) (2012) 5542–5556.

[35] F. Ballarin, E. Faggiano, S. Ippolito, A. Manzoni, A. Quarteroni, G. Rozza, R. Scrofani, Fast simulations of patient-specific haemodynamics of coronary artery bypass grafts based on a POD-Galerkin method and a vascular shape parametrization, Journal of Computational Physics 315 (2016) 609–628.

[36] M. Dehghan, M. Abbaszadeh, The use of proper orthogonal decomposition (POD) meshless RBF-FD technique to simulate the shallow water equations, Journal of Computational Physics 351 (2017) 478–510.

[37] K. Li, T.-Z. Huang, L. Li, S. Lanteri, L. Xu, B. Li, A reduced-order discontinuous Galerkin method based on POD for electromagnetic simulation, IEEE Transactions on Antennas and Propagation 66 (1) (2018) 242–254.

[38] K. Li, T.-Z. Huang, L. Li, S. Lanteri, POD-based model order reduction with an adaptive snapshot selection for a discontinuous Galerkin approximation of the time-domain Maxwell's equations, Journal of Computational Physics 396 (2019) 106–128.

[39] M. Guo, J. S. Hesthaven, Data-driven reduced order modeling for time-dependent problems, Computer Methods in Applied Mechanics and Engineering 345 (2019) 75–99.

[40] S. Hijazi, G. Stabile, A. Mola, G. Rozza, Data-driven POD-Galerkin reduced order model for turbulent flows, Journal of Computational Physics 416 (2020) 109513. doi:https://doi.org/10.1016/j.jcp.2020.109513.

[41] F. Stefania, M. Andrea, POD-DL-ROM: Enhancing deep learning-based reduced order models for nonlinear parametrized PDEs by proper orthogonal decomposition, Computer Methods in Applied Mechanics and Engineering 388 (2022) 114181. doi:https://doi.org/10.1016/j.cma.2021.114181.

[42] H. Xia, Z. Luo, A POD-based–optimized finite difference CN-extrapolated implicit scheme for the 2-D viscoelastic wave equation, Mathematical Methods in the Applied Sciences 40 (18) (2017) 6880–6890.

[43] X. Zhang, P. Zhang, A reduced high-order compact finite difference scheme based on proper orthogonal decomposition technique for KdV equation, Applied Mathematics and Computation 339 (2018) 535–545.

[44] B. Xu, X. Zhang, An efficient high-order compact finite difference scheme based on proper orthogonal decomposition for the multi-dimensional parabolic equation, Advances in Difference Equations 2019 (1) (2019) 341. doi:https://doi.org/10.1186/s13662-019-2273-3.

[45] O. Lass, S. Volkwein, POD-Galerkin schemes for nonlinear elliptic-parabolic systems, SIAM Journal on Scientific Computing 35 (3) (2013) A1271–A1298.

[46] S. Ullmann, M. Rotkvic, J. Lang, POD-Galerkin reduced-order modeling with adaptive finite element snapshots, Journal of Computational Physics 325 (2016) 244–258.

[47] E. N. Karatzas, F. Ballarin, G. Rozza, Projection-based reduced order models for a cut finite element method in parametrized domains, Computers & Mathematics with Applications 79 (3) (2020) 833–851.

[48] S. Lorenzi, A. Cammi, L. Luzzi, G. Rozza, POD-Galerkin method for finite volume approximation of Navier–Stokes and RANS equations, Computer Methods in Applied Mechanics and Engineering 311 (2016) 151–179.

[49] G. Stabile, G. Rozza, Finite POD-Galerkin stabilised reduced order methods for the parametrised incompressible Navier-Stokes equations, Computers & Fluids 173 (2018) 273–284.

[50] L. Fezoui, S. Lanteri, S. Lohrengel, S. Piperno, Convergence and stability of a discontinuous Galerkin time-domain method for the 3-D heterogeneous Maxwell equations on unstructured meshes, ESAIM: Mathematical Modelling and Numerical Analysis 39 (6) (2005) 1149–1176.

[51] J. Viquerat, M. Klemm, S. Lanteri, C. Scheid, Theoretical and numerical analysis of local dispersion models coupled to a discontinuous Galerkin time-domain method for Maxwell's equations, Tech. rep. (2013).

[52] H. Fahs, S. Lanteri, A high-order non-conforming discontinuous Galerkin method for time-domain electromagnetics, Journal of Computational and Applied Mathematics 234 (4) (2010) 1088–1096.

[53] V. Dolean, H. Fahs, L. Fezoui, S. Lanteri, Locally implicit discontinuous Galerkin method for time domain electromagnetics, Journal of Computational Physics 229 (2) (2010) 512–526.

[54] Z. Luo, H. Li, Y. Zhou, X. Huang, A reduced FVE formulation based on POD method and error analysis for two-dimensional viscoelastic problem, Journal of Mathematical Analysis and Applications 385 (1) (2012) 310–321.

[55] Z. Luo, J. Gao, A POD reduced-order finite difference time-domain extrapolating scheme for the 2D Maxwell equations in a lossy medium, Journal of Mathematical Analysis and Applications 444 (1) (2016) 433–451.

[56] K. Kunisch, S. Volkwein, Galerkin proper orthogonal decomposition methods for parabolic problems, Numerische Mathematik 90 (1) (2001) 117–148.

[57] H. C. van de Hulst, Light scattering by small particles, Dover Pulibcations, 1981.

[58] B. Grześkiewicz, K. Ptaszyński, M. Kotkowiak, Near and far-field properties of nanoprisms with rounded edges, Plasmonics 9 (3) (2014) 607–614.